



Mamba Goes HoME: Hierarchical Soft Mixture-of-Experts for 3D Medical Image Segmentation

Szymon Plotka^{1*} Maciej Chrabaszcz² Gizem Mert³
Ewa Szczurek^{1,3} Arkadiusz Sitek^{4,5}

¹ University of Warsaw

² Warsaw University of Technology

³ Institute of AI for Health, Helmholtz Munich

⁴ Massachusetts General Hospital

⁵ Harvard Medical School

Abstract

In recent years, artificial intelligence has significantly advanced medical image segmentation. However, challenges remain, including efficient 3D medical image processing across diverse modalities and handling data variability. In this work, we introduce Hierarchical Soft Mixture-of-Experts (HoME), a two-level token-routing layer for efficient long-context modeling, specifically designed for 3D medical image segmentation. Built on the Mamba state-space model (SSM) backbone, HoME enhances sequential modeling through sparse, adaptive expert routing. The first stage employs a Soft Mixture-of-Experts (SMoE) layer to partition input sequences into local groups, routing tokens to specialized per-group experts for localized feature extraction. The second stage aggregates these outputs via a global SMoE layer, enabling cross-group information fusion and global context refinement. This hierarchical design, combining local expert routing with global expert refinement improves generalizability and segmentation performance, surpassing state-of-the-art results across datasets from the three most commonly used 3D medical imaging modalities and data quality.

1 Introduction

Three-dimensional (3D) medical image segmentation lies at the core of computer-aided diagnosis, image-guided interventions, and treatment planning across modalities such as Computed Tomography (CT), Magnetic Resonance Imaging (MRI), and Ultrasound (US) [6]. A key characteristic of medical imaging data is its hierarchical structure: local patterns, such as tumor lesions, are embedded within larger anatomical structures like organs, which themselves follow a consistent global arrangement. We hypothesize that *models capable of capturing these local-to-global spatial hierarchies in 3D medical data can enhance segmentation performance and yield latent representations that generalize effectively across diverse imaging modalities.*

Convolutional Neural Networks provide local feature extraction with linear complexity in the number of input pixels, but their limited receptive fields hinder their ability to capture global spatial patterns [36, 47, 18, 42]. In contrast, Vision Transformers (ViTs) [14, 5, 26] leverage global attention mechanisms to model long-range dependencies. Yet, their quadratic complexity in the number of tokens makes them computationally costly for high-resolution 3D data, posing significant challenges for

*Correspondence to: Szymon Plotka (PLOTKASZYMON@GMAIL.COM)

scalability. Moreover, while many ViT-based models [43, 16, 32, 25, 22, 39] incorporate multi-scale feature extraction and attention mechanisms, they still struggle to effectively aggregate fine-to-coarse semantic information, particularly in dense prediction tasks such as volumetric segmentation. Although these models demonstrate improved performance, they do not explicitly model global and local spatial patterns along with their mutual arrangement. Modeling the transition from local to global patterns requires processing long sequences and capturing long-range dependencies, imposing prohibitive memory and computational demands on current architectures.

Recently, State Space Models (SSMs), such as Mamba [17, 13], have emerged as efficient alternatives to ViTs by offering linear complexity in the number of tokens to capture long-range dependencies, including in 3D medical imaging [44, 38, 24, 10, 41]. Although SSMs effectively capture global context with lower computational cost than attention-based methods, they are not inherently designed to adaptively handle diverse local patterns in medical data. Efficient management of such local patterns in complex, multi-scale data while maintaining scalability is achieved through Mixture-of-Experts (MoE) frameworks, which dynamically route features to specialized subnetworks. MoE-based methods gained prominence across domains such as language modeling [4, 46, 21], vision tasks [33, 49, 35, 12, 15], multimodal learning [28, 8, 45], and medical applications [20, 11, 40, 32]. However, combining the global efficiency of SSMs with the localized adaptability of MoE remains largely unexplored, particularly in 3D medical imaging, where balancing efficiency and generalization across multi-modal datasets under resource constraints is paramount.

To address these challenges, we introduce the first-in-class model that smoothly integrates Mamba with hierarchical, Soft MoE in a multi-stage network for local-to-global pattern modeling and 3D image segmentation with unprecedented memory and compute efficiency. Specifically, our contributions are as follows:

1. We introduce **Hierarchical Soft Mixture-of-Experts (HoME)**, a two-level, token-routing MoE layer for efficient capture of local-to-global pattern hierarchies, where tokens are grouped and routed to local experts in the first SMoE level, then aggregated and passed via a global SMoE in the second level,
2. We design a unified architectural block that integrates Mamba’s SSMs with HoME, combining memory-efficient long-sequence processing with hierarchical expert routing,
3. We embed the above novel solutions into a multi-stage U-shaped architecture, called **Mamba-HoME**, specifically designed for 3D medical image segmentation, where the integration of hierarchical memory and state-space modeling enhances contextual representation across spatial and depth dimensions.

Through comprehensive experiments on four publicly available datasets, PANORAMA [2], AMOS2022 [19], FeTA2022 [31], and MVSeg2023 [9], as well as one in-house CT dataset, we demonstrate that Mamba-HoME outperforms current state-of-the-art methods in both segmentation accuracy and computational efficiency, while generalizing effectively across three major 3D medical imaging modalities: CT, MRI, and US.

2 Methodology

2.1 Hierarchical Soft Mixture-of-Experts (HoME) Layer

Following the integration of SSM, Mamba, within the broader Mamba-HoME architecture, we introduce the HoME layer (see Figure 1(b)), which enhances feature processing through a hierarchical two-level structure. The HoME layer, illustrated within the Mamba-based encoder, builds on the SMoE framework [33] with a two-level SMoE hierarchy that efficiently processes grouped input tokens and enables robust inter-group information sharing. It comprises three key steps: (1) grouped slot assignment for token processing, (2) first-level MoE processing for local feature extraction, and (3) second-level MoE refinement for global feature extraction, allowing inter-group communication.

Grouped Slot Assignment. In hierarchical vision encoders, particularly for dense 3D inputs (e.g., volumetric data), the sequence length is highest in early stages due to large spatial resolutions. Global expert routing on these long sequences causes high computational and memory costs, as each token is compared to all expert slots, yielding a complexity of $\mathcal{O}(N \cdot M_s)$, where N is the sequence length and M_s is the number of expert slots. To address this scalability bottleneck, we propose Grouped

Slot Assignment, a locality-aware routing mechanism that divides the input sequence into groups and performs soft assignment independently per group.

At stage $t \in \{1, \dots, T\}$, the input is a 3D feature tensor $x \in \mathbb{R}^{B \times N \times d}$, where B is the batch size, N is the sequence length, and d is the feature dimension. The sequence is partitioned into $G_t = \lceil N/K_t \rceil$ non-overlapping groups, each containing at most K_t tokens.

The group size K_t is defined as a monotonically decreasing function of the stage index t , i.e.,

$$K_t = K_1 \cdot \rho^{t-1}, \quad \text{where } 0 < \rho < 1.$$

This formulation reflects finer-grained token grouping at deeper stages. If N is not divisible by K_t , the sequence is zero-padded to length $N' = G_t \cdot K_t$, yielding a padded tensor $\hat{x} \in \mathbb{R}^{B \times N' \times d}$.

Each group $x_g \in \mathbb{R}^{B \times K_t \times d}$ is routed independently. Assignment logits are computed via a dot product between each token and learnable expert-specific slot embeddings $E_{\text{slots}} \in \mathbb{R}^{E_t \times S_t \times d}$, where E_t is the number of experts and S_t is the number of slots per expert, indexed by $s \in \{1, \dots, S_t\}$. The logits are computed as:

$$S_{b,g,k,e,s} = \sum_{j=1}^d x_{b,g,k,j} \cdot E_{e,s,j}, \quad (1)$$

where $S \in \mathbb{R}^{B \times G_t \times K_t \times E_t \times S_t}$ contains the assignment logits for routing tokens to expert slots at stage $t \in \{1, \dots, T\}$.

An optional binary mask $M \in \{0, 1\}^{B \times N}$, indicating valid (unpadded) tokens, is extended to $\hat{M} \in \{0, 1\}^{B \times N'}$ after padding. To prevent padded tokens from affecting expert assignment, the logits for invalid tokens are masked by setting:

$$S_{b,g,k,e,s} = \begin{cases} S_{b,g,k,e,s}, & \text{if } \hat{M}_{b,gK_t+k} = 1, \\ -\infty, & \text{otherwise,} \end{cases} \quad (2)$$

where $S \in \mathbb{R}^{B \times G_t \times K_t \times E_t \times S_t}$ contains the assignment logits for routing tokens to expert slots.

Here, $b \in \{1, \dots, B\}$ indexes the batch, $g \in \{1, \dots, G_t\}$ the group, $k \in \{1, \dots, K_t\}$ the token within a group, $e \in \{1, \dots, E_t\}$ the expert, $s \in \{1, \dots, S_t\}$ the slot per expert, $j \in \{1, \dots, d\}$ the feature dimension, and $t \in \{1, \dots, T\}$ the stage.

The logits $S \in \mathbb{R}^{B \times G_t \times K_t \times E_t \times S_t}$ are rearranged by combining the expert and slot dimensions into a single dimension of size $M_t = E_t \cdot S_t$, where the combined index $m \in \{1, \dots, M_t\}$ corresponds to expert-slot pairs (e, s) via $m = (e - 1)S_t + s$. This yields logits $S \in \mathbb{R}^{B \times G_t \times K_t \times M_t}$. The softmax function is applied along the combined dimension to compute assignment weights:

$$A_{b,g,k,m} = \frac{\exp(S_{b,g,k,m})}{\sum_{m'=1}^{M_t} \exp(S_{b,g,k,m'})}, \quad A \in \mathbb{R}^{B \times G_t \times K_t \times M_t}. \quad (3)$$

Each slot representation is computed as a weighted aggregation of tokens within its group:

$$\tilde{x}_{b,g,e,s,j} = \sum_{k=1}^{K_t} A_{b,g,k,m} \cdot x_{b,g,k,j}, \quad \text{where } m = (e - 1)S_t + s, \quad \tilde{x} \in \mathbb{R}^{B \times G_t \times E_t \times S_t \times d}. \quad (4)$$

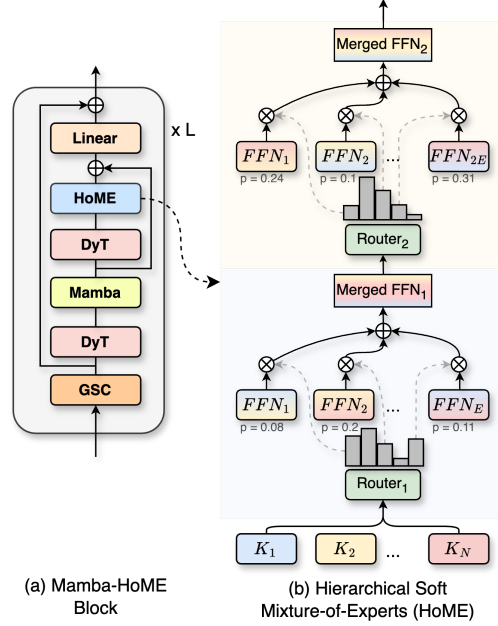


Figure 1: An overview of the Mamba-HoME Block and HoME layer design. (a) The Mamba-HoME Block integrates a Gated Spatial Convolution (GSC), an SSM model (Mamba) for efficient processing of local features and long sequences, and hierarchical expert processing (HoME). As a normalization layer, we use Dynamic Tanh (DyT). (b) The HoME layer operates on grouped input tokens K_1, K_2, \dots, K_N , using a two-level hierarchical structure. First-level gating, $Router_1$, routes grouped tokens to experts $FFN_1, FFN_2, \dots, FFN_E$ for local feature extraction with probabilities p , followed by merging. Second-level gating, $Router_2$, enables inter-group communication by routing group slots to additional experts $FFN_1, FFN_2, \dots, FFN_{2E}$ with probabilities p before final aggregation.

Inner group routing reduces the computational complexity of token-to-expert assignment by processing tokens in $G_t = \lceil N/K_t \rceil$ groups, each of size K_t , compared to processing all N tokens globally. This design yields a complexity of $\mathcal{O}(G_t \cdot K_t \cdot M_t \cdot d)$ for assigning K_t tokens to $M_t = E_t \cdot S_t$ expert-slot pairs across G_t groups, compared to $\mathcal{O}(N \cdot M_t \cdot d)$ for global assignment, where $G_t \ll N$ for large K_t . Grouping enhances efficiency and memory usage through localized computations, while preserving local spatial coherence for 3D inputs. Moreover, restricting expert interactions to local groups promotes expert specialization and supports scalable, hierarchical token-to-expert assignment.

Hierarchical Expert Processing. Let $\tilde{x} \in \mathbb{R}^{B \times G_s \times M_s \times d}$ denote the input slot representations, where B is the batch size, G_s is the number of groups, M_s is the number of slots per group, and d is the dimensionality of each slot. The first level routes slots within each group to a subset of E_s Feed-Forward Network (FFN) experts, leveraging specialization to enhance efficiency and local feature quality. This produces group-specific outputs of shape $M_s \times d$ that preserve the original slot structure by maintaining a one-to-one correspondence between input and output slots within each group. For each group $g \in \{1, \dots, G_s\}$, the gating network computes routing weights for E_s FFN experts ($\text{FFN}_1, \text{FFN}_2, \dots, \text{FFN}_{E_s}$):

$$\text{Router}_1(\tilde{x}_{b,g}; \theta_{\text{gate}}^{(1)}) = \text{softmax} \left(\text{MLP} \left(\frac{1}{M_s} \sum_{m=1}^{M_s} \tilde{x}_{b,g,m} \right) \right), \quad (5)$$

where $\tilde{x}_{b,g} = \{\tilde{x}_{b,g,m}\}_{m=1}^{M_s} \in \mathbb{R}^{M_s \times d}$ denotes the slots in group g for batch element b , $\tilde{x}_{b,g,m} \in \mathbb{R}^d$, $\theta_{\text{gate}}^{(1)}$ are the gating parameters, and softmax normalizes over the expert dimension, yielding $\text{Router}_1 \in \mathbb{R}^{E_s}$. Each expert, implemented as an $\text{FFN}_e : \mathbb{R}^{M_s \times d} \rightarrow \mathbb{R}^{M_s \times d}$, processes the group's slots independently. The output for expert $e \in \{1, \dots, E_s\}$ is:

$$y_{b,g,e} = [\text{Router}_1(\tilde{x}_{b,g}; \theta_{\text{gate}}^{(1)})]_e \cdot \text{FFN}_e(\tilde{x}_{b,g}) \quad (6)$$

and the aggregated output is: $y_{b,g}^{(1)} = \sum_{e=1}^{E_s} y_{b,g,e}$, where $y^{(1)} \in \mathbb{R}^{B \times G_s \times M_s \times d}$.

Dynamic Slot Refinement. The second level reshapes the group-slot structure into a sequence and routes it to second-level experts (E_2), modeling cross-group dependencies to produce a globally informed representation. The tensor $y^{(1)}$ is transformed into $\tilde{y} \in \mathbb{R}^{B \times (G_s M_s) \times d}$ before being passed through the second-level experts. The gating network computes routing weights for E_2 FFN experts ($\text{FFN}_1, \text{FFN}_2, \dots, \text{FFN}_{E_2}$):

$$\text{Router}_2(\tilde{y}; \theta_{\text{gate}}^{(2)}) = \text{softmax}(\text{MLP}(\tilde{y})), \quad (7)$$

where $\theta_{\text{gate}}^{(2)}$ are the gating parameters, and softmax normalizes over the expert dimension, producing $\text{Router}_2 \in \mathbb{R}^{B \times (G_s M_s) \times E_2}$. Each second-level expert, implemented as $\text{FFN}_{e_2} : \mathbb{R}^{(G_s M_s) \times d} \rightarrow \mathbb{R}^{(G_s M_s) \times d}$, processes \tilde{y} . The output for expert $e_2 \in \{1, \dots, E_2\}$ is:

$$y_{b,e_2} = \left(\text{Router}_2(\tilde{y}_b; \theta_{\text{gate}}^{(2)}) \right)_{e_2} \cdot \text{FFN}_{e_2}(\tilde{y}_b) \quad (8)$$

and outputs are aggregated into: $y^{(2)} = \sum_{e_2=1}^{E_2} y_{b,e_2}$, where $y^{(2)} \in \mathbb{R}^{B \times (G_s M_s) \times d}$.

The final stage reconstructs a structured output using an attention-based combination to emphasize relevant slots and remove padding, yielding a compact, task-aligned representation. The tensor $y^{(2)}$ is reshaped to $\mathbb{R}^{B \times G_s \times M_s \times d}$. For batch element b , group g , and slot $k \in \{1, \dots, M_s\}$, the output is:

$$y_{b,g,k} = \sum_{m=1}^{M_s} A_{b,g,k,m} \cdot y_{b,g,m}^{(2)}, \quad (9)$$

where $y_{b,g,m}^{(2)} \in \mathbb{R}^d$, and $A_{b,g,k,m} \in [0, 1]$ are attention weights satisfying $\sum_{m=1}^{M_s} A_{b,g,k,m} = 1$. The final output is: $\hat{y} \in \mathbb{R}^{B \times N \times d}$, where $N \leq G_s M_s$ is the number of valid slots, corresponding to K_1, K_2, \dots, K_N (see Figure 1(b)).

2.2 Mamba-HoME Block

Figure 1(a) provides an overview of the proposed Mamba-HoMEB. The Mamba-HoMEB extends the Mamba layer by incorporating hierarchical downsampling, Gated Spatial Convolution (GSC) layers

[44], and a Hierarchical Soft Mixture-of-Experts (HoME) layer (see Sec. 2.1). To improve gradient stability and computational efficiency in SSMs, we use Dynamic Tanh (DyT) [48] normalization. Unlike LayerNorm [7], it avoids costly mean and variance computations, reducing overhead while maintaining $\mathcal{O}(Bd)$ complexity. DyT accelerates training and validation with performance on par with normalization-based alternatives.

Given a 3D input volume $x \in \mathbb{R}^{B \times C \times D \times H \times W}$, the initial feature map $x_0 \in \mathbb{R}^{B \times 48 \times \frac{D}{2} \times \frac{H}{2} \times \frac{W}{2}}$ is extracted by a stem layer. This feature map x_0 is then passed through each Mamba-HoMEB and its corresponding downsampling layers. The representations for the i -th Mamba-HoMEB are given by:

$$\hat{x}_i^l = f_{\text{GSC}}(x_i^l), \quad \tilde{x}_i^l = f_{\text{Mamba}}(f_{\text{DyT}}(\hat{x}_i^l)) + \hat{x}_i^l, \quad x_i^{l+1} = f_{\text{Linear}}(f_{\text{HoME}}(f_{\text{DyT}}(\tilde{x}_i^l))) + \tilde{x}_i^l, \quad (10)$$

where $l \in \{0, 1, \dots, L_i - 1\}$, L_i is the total number of layers, f_{GSC} denotes Gated Spatial Convolution, f_{Mamba} the Mamba layer, f_{DyT} Dynamic Tanh, f_{HoME} the HoME layer, and f_{Linear} Linear layer, respectively. The HoME layer operates hierarchically at each encoder stage $t \in \{1, \dots, T\}$, with the number of first-level experts denoted by E_t and the group size (i.e., the number of tokens processed jointly within each local group) denoted by K_t . The number of experts E_t increases monotonically with stage depth, reflecting increased specialization ($E_1 < E_2 < \dots < E_T$), while the group size K_t decreases, enabling progressively finer-grained processing ($K_1 > K_2 > \dots > K_T$). In addition to the first-level experts, each stage employs a second-level expert set $E_{2,t}$, which scales proportionally with E_t , i.e., $E_{2,t} = 2E_t$. This second level facilitates global context integration across groups, enhancing inter-group communication. The HoME operation at each stage thus combines local expert routing with global feature aggregation (see Sec. 2.1).

2.3 The Mamba-HoME Architecture

Building upon SegMamba [44], we introduce a U-shaped encoder-decoder network, called **Mamba-HoME**, designed for 3D medical image segmentation. It leverages a Mamba-based encoder backbone to capture long-range dependencies and local features efficiently. The model processes an input 3D volume $x \in \mathbb{R}^{B \times C \times D \times H \times W}$ to generate a segmentation mask $y \in \mathbb{R}^{B \times C \times D \times H \times W}$, where B denotes the batch size and C the number of channels, while D, H, W are spatial dimensions. The encoder comprises T hierarchical stages, each extracting features at progressively coarser resolutions. In the i -th stage, the feature map is denoted as $F_i \in \mathbb{R}^{B \times C_i \times D_i \times H_i \times W_i}$, and is transformed as:

$$F_{i+1} = \text{Downsample}_i(\text{Mamba-HoMEB}_i(F_i)), \quad (11)$$

where Downsample_i is a convolutional operation that reduces spatial dimensions by a factor of 2 ($D_{i+1} = \lfloor D_i/2 \rfloor$, $H_{i+1} = \lfloor H_i/2 \rfloor$, $W_{i+1} = \lfloor W_i/2 \rfloor$) and doubles the channel depth ($C_{i+1} = 2C_i$). The Mamba-HoMEB_i integrates convolutional modules for local feature enhancement with Mamba-based state-space mechanisms for global context modeling. The encoder produces feature maps $\{F_1, F_2, \dots, F_T\}$, with F_T as the bottleneck feature.

The decoder mirrors the encoder with $T - 1$ upsampling stages, reconstructing the segmentation mask from the bottleneck feature $U_T = F_T$. For stage $t = T - 1, \dots, 1$, the decoder computes:

$$U_s = \text{UpBlock}_t(x_t^{l_t} \oplus \text{Up}(d_{t+1})), \quad (12)$$

where Up upsamples the spatial dimensions to (D_t, H_t, W_t) with $D_t = \frac{D}{2^t}$, $H_t = \frac{H}{2^t}$, and $W_t = \frac{W}{2^t}$. Here, $x_t^{l_t} \in \mathbb{R}^{B \times C_t \times H_t \times W_t \times D_t}$ represents the skip connection from the encoder's t -th stage, and \oplus denotes feature concatenation along the channel dimension. The UpBlock_t refines the concatenated features, mapping them to the target resolution for the next decoding stage.

The computational complexity of Mamba-HoME scales as $\mathcal{O}(BNd)$ for the Mamba layer and $\mathcal{O}(BG_t(E_{1,t} + E_{2,t})T_t d)$ for the HoME layer at stage t , where N is the token sequence length, G_t is the number of groups, and $E_{1,t} + E_{2,t}$ reflects the total experts. Compared to Transformer-based models ($\mathcal{O}(BN^2d)$), this linear scaling in N ensures efficiency for large 3D volumes (e.g., $N \approx 10^6$ tokens), with HoME adding a modest overhead proportional to the expert count.

3 Experiments

In this section, we evaluate the performance of the proposed Mamba-HoME against state-of-the-art methods for 3D medical image segmentation (see Sec. 3.2). We perform an ablation study to understand the importance of different configurations and parameters of Mamba-HoME. Moreover, we compare the segmentation performance of Mamba-HoME trained from scratch with a version pretrained using a supervised learning approach (see Sec. 3.3).

Finally, in Sec. 3.4, we investigate how Mamba-HoME generalizes to new modalities. The best results are **bolded**, while the second-best results are underlined.

3.1 Datasets

Pre-training. We use publicly available datasets covering two imaging modalities: AbdomenAtlas1.1 [34, 22] for CT scans and TotalSegmentator [1] for MRI scans, both containing voxel-wise annotated masks of abdominal anatomical structures.

Training and fine-tuning. We use datasets covering three primary 3D medical imaging modalities: PANORAMA (CT) [2], AMOS (CT and MRI) [19], FeTA 2022 (MRI, fetal) [31], MVSeg 2023 (3D US) [9], and an in-house CT dataset.

Detailed descriptions of the datasets and the experimental setup are provided in Appendix A and Appendix B, respectively.

3.2 Comparison with state-of-the-art methods

We compare our proposed Mamba-HoME with eight state-of-the-art approaches for 3D medical image segmentation, including uC 3DU-Net [18], Swin SMT [32], VoCo-B [43], SuPreM [23], Hermes [16], Swin UNETR [39], VSmTrans [25], and SegMamba (baseline) [44], across four publicly available and one in-house 3D datasets encompassing diverse anatomical structures and imaging modalities, such as CT, MRI, and 3D US. Both

VoCo-B and SuPreM are pretrained on large-scale CT scans using self-supervised and supervised learning approaches, respectively. Additionally, we evaluate Mamba-HoME trained from scratch against Mamba-HoME pretrained with a supervised learning approach to assess the impact of pretraining on segmentation performance. Detailed quantitative and more qualitative results for benchmarking datasets are provided in Appendix C, and Appendix F, respectively.

Table 1: Segmentation performance on the PANORAMA and in-house test sets. PDAC and P denote pancreatic ductal adenocarcinoma and pancreas, respectively. (*) indicates a pre-trained model.

Methods	DSC (%) \uparrow		mDSC (%) \uparrow	mHD95 (mm) \downarrow	Params (M) \downarrow	GPU (G) \downarrow	IS(\dagger) \downarrow
	PDAC	P					
VoCo-B (*)	40.5	86.3	71.6	89.2	53.0	17.1	1.5
Hermes	48.2	87.8	75.1	9.3	<u>44.5</u>	17.4	1.9
Swin SMT	49.4	87.0	75.0	32.9	170.8	15.8	1.3
VSmTrans	50.3	87.2	75.4	33.6	47.6	<u>11.1</u>	1.7
uC 3DU-Net	52.0	88.2	76.6	8.1	21.7	13.6	1.0
Swin UNETR	46.3	87.4	74.2	74.3	72.8	17.1	1.5
SegMamba	49.7	88.5	76.0	14.1	66.8	10.1	<u>1.2</u>
SuPreM (*) \dagger	51.7	<u>88.3</u>	76.6	<u>4.4</u>	62.2	17.1	1.5
Mamba-HoME	<u>54.8</u>	<u>88.3</u>	<u>77.5</u>	6.9	170.5	11.3	1.5
Mamba-HoME (*)	56.7	88.5	78.2	4.1	170.5	11.3	1.5

\dagger Please note, SuPreM was partially pre-trained on a subset of the PANORAMA test set, including the Pancreas MSD and NIH datasets, which may result in an unfair comparison.

\dagger Inference speed (IS) is standardized to 1.0 = 1770 ms.

Table 2: Segmentation performance and generalizability of the Mamba-HoME and previous models on the AMOS dataset (CT and MRI). CT: trained solely on the AMOS CT subset; CT \rightarrow MRI: pre-trained on the AMOS CT subset and fine-tuned on the AMOS MRI subset; MRI: trained solely on the AMOS MRI subset; CT+MRI: trained on both subsets. (*) denotes a pre-trained model.

Method	mDSC (%) \uparrow				mHD95 (mm) \downarrow			
	CT	CT \rightarrow MRI	MRI	CT + MRI	CT	CT \rightarrow MRI	MRI	CT + MRI
Hermes	85.3	<u>84.8</u>	80.7	82.9	<u>40.5</u>	11.9	13.9	36.1
Swin SMT	85.7	83.2	63.2	81.2	91.4	21.0	45.1	98.9
VSmTrans	85.3	84.0	74.6	78.0	178.7	30.1	30.6	102.1
uC 3DU-Net	82.7	84.5	68.6	84.1	47.3	15.4	<u>16.3</u>	<u>34.9</u>
Swin UNETR	84.3	84.2	75.0	81.2	94.7	28.4	30.7	84.7
SegMamba	86.0	84.4	80.2	84.7	98.9	14.7	33.1	64.2
SuPreM (*)	86.0	83.9	70.3	83.5	66.0	14.8	52.1	48.2
Mamba-HoME	<u>86.3</u>	<u>84.8</u>	<u>81.0</u>	<u>85.1</u>	45.0	16.0	32.5	54.8
Mamba-HoME (*)	87.3	85.0	82.3	86.4	32.0	<u>13.3</u>	19.5	<u>27.7</u>

\dagger SuPreM was pre-trained on the AMOS CT training set, while VoCo-B was pre-trained on both the training and validation sets, and we removed VoCo-B from the benchmark as it may lead to an unfair comparison.

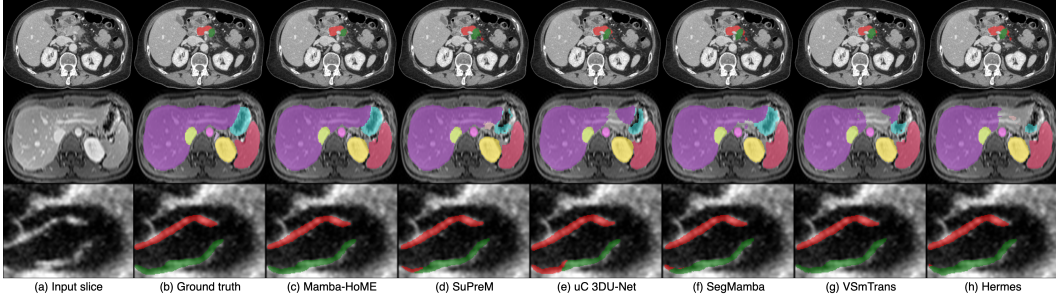


Figure 2: Qualitative segmentation results comparing our proposed Mamba-HoME with the next five top-performing methods across three modalities (CT, MRI, and US).

Quantitative results. Results for our proposed method, Mamba-HoME, for PANORAMA and in-house datasets are in Table 1. Results for other modalities AMOS-CT/MRI, FeTA 2022 (fetal MRI), and MVSeg 2023 (3D US) are presented in Table 2, Table 3, and Table 4, respectively.

Our proposed method, Mamba-HoME, demonstrates consistent performance improvements over state-of-the-art baselines across all benchmark datasets and three imaging modalities.

Evaluated under two distinct configurations (scratch and pre-trained), Mamba-HoME achieves superior segmentation accuracy, obtaining the best results in terms of both DSC and HD95. Despite having a relatively large number of parameters (170.5M) compared to competing methods, it exhibits low GPU memory usage during inference (Table 1), a crucial advantage for processing high-resolution 3D medical data. Although inference is approximately 30% slower than the baseline, the performance gains present a compelling trade-off between accuracy and efficiency. The Wilcoxon signed-rank test indicates a significant difference between Mamba-HoME and other state-of-the-art methods, using $p < 0.05$ as the significance threshold.

Qualitative results. Figure 2 presents a qualitative comparison of our proposed Mamba-HoME method against the five top-performing baselines across three primary 3D medical imaging modalities: CT, MRI, and US. These modalities exhibit different organ contrasts, noises, or resolutions. Mamba-HoME demonstrates consistent improvements in segmentation quality across these scenarios. In the first row, it effectively handles small and closely located structures, showing precise boundary delineation while reducing common artifacts seen in baseline predictions. The second row highlights its capability to accurately segment organs of various shapes and sizes, even under low image quality conditions, with reduced susceptibility to over- or under-segmentation. The third row illustrates Mamba-HoME’s robustness in handling noisy and low-resolution data, maintaining clear and anatomically accurate boundaries.

3.3 Ablation studies

In this section, we investigate the impact of several factors on the performance of Mamba-HoME: (1) the parameters of HoME, including the number of experts in the first (E_1) and second (E_2) levels, the number of the group size (K), and the number of slots per expert (S), and (2) impact of the

Table 3: 5-fold cross-validation of segmentation performance on the FeTA 2022 training set. (*) indicates a pre-trained model.

Methods	mDSC \uparrow (%)	mHD95 \downarrow (mm)
VoCo-B (*)	86.0	4.0
Hermes	86.5	4.0
Swin SMT	85.9	2.4
VSmTrans	86.1	2.3
uC 3DU-Net	85.9	3.5
Swin UNETR	86.2	2.5
SegMamba	85.9	3.5
SuPreM (*)	85.3	3.6
Mamba-HoME	87.5	2.1
Mamba-HoME (*)	87.7	2.0

Table 4: Segmentation performance on the MVSeg test set. (*) indicates a pre-trained model.

Methods	mDSC \uparrow (%)	mHD95 \downarrow (mm)
Hermes	83.5	13.3
Swin SMT	83.4	17.2
VSmTrans	84.4	17.4
uC 3DU-Net	83.9	13.4
Swin UNETR	84.4	13.1
SegMamba	83.8	15.6
SuPreM (*)	84.3	12.9
Mamba-HoME	84.8	12.6
Mamba-HoME (*)	85.0	12.2

pre-trained model in supervised learning approach. For each configuration, we evaluate the number of model parameters, GPU memory usage, and average DSC across three datasets. More details on ablation studies can be found in the Appendix E.

Effect of the number of experts. We evaluate the impact of varying the number of experts at each encoder stage (t), where $t \in \{0, 1, 2, 3\}$, in a two-level HoME layer. For a fair comparison, we maintain a constant group size $K \in \{2048, 1024, 512, 256\}$ and set the number of slots to $S = 4$. Table 5 shows that the configuration with expert counts $E_1 = [4, 8, 12, 16]$ at the first level and $E_2 = [8, 16, 24, 32]$ at the second level of HoME achieves the best trade-off between segmentation performance and parameter efficiency, requiring the fewest parameters and the lowest usage of GPU memory.

Effect of the number of groups. We evaluate the impact of the number of groups at each encoder stage (t), where $t \in \{0, 1, 2, 3\}$, in a two-level HoME layer. For a fair comparison, we use a constant number of experts, $E_1 \in \{4, 8, 12, 16\}$ and $E_2 \in \{8, 16, 24, 32\}$, with a fixed number of slots, $S = 4$. Table 6 demonstrates that Mamba-HoME achieves optimal performance with group sizes $K \in \{2048, 1024, 512, 256\}$, while yielding the second-lowest usage of GPU memory.

Effect of the number of slots per expert. We show the impact of the number of slots (S) per expert (E) at each encoder stage (t), where $t \in \{0, 1, 2, 3\}$, in a two-level HoME layer. For a fair comparison, we use a constant number of experts, $E_1 \in \{4, 8, 12, 16\}$ and $E_2 \in \{8, 16, 24, 32\}$, and number of groups, $K \in \{2048, 1024, 512, 256\}$. Table 7 shows that Mamba-HoME achieves optimal performance at $S = 4$ across all evaluated datasets, representing a sweet spot for the number of slots per expert. Testing variations in the number of slots per expert ($S \in \{1, 2, 8\}$) shows no significant performance improvements, with other slot counts yielding suboptimal performance, while keeping the number of parameters and GPU memory constant.

Effect of Dynamic Tanh normalization in SSMs. While DyT accelerates CNN and Transformer-based methods, we evaluate its effectiveness in an SSM-based model compared to LayerNorm. As shown in Table 8, there is no significant difference in segmentation performance, but DyT improves training and inference speed by approximately 6% based on experimental runtime measurements².

Impact of supervised pre-training.

We evaluate the efficacy of our proposed Mamba-HoME model, pre-trained under a supervised learning paradigm. The evaluation contains three primary 3D medical imaging modalities and various anatomical regions. Overall, Mamba-HoME outperforms state-of-the-art results, surpassing existing methods in terms of both the DSC and the HD95 across all evaluated datasets. These quantitative outcomes underscore the effectiveness of supervised pre-training in enhancing segmentation accuracy and robustness. A key attribute of Mamba-HoME is its cross-modal generalization,

Table 5: Qualitative segmentation performance on the varying number of experts at each encoder stage.

Experts (E) ↓	Params (M) ↓	GPU (G) ↓	mDSC (%) ↑		
			PANORAMA	AMOS-CT	FeTA
[4, 8, 12, 16]*	170.5	12.8	77.5	86.3	87.5
[8, 16, 24, 48]	254.1	13.5	76.3	86.2	87.3
[8, 16, 24, 48]*	274.2	13.5	76.0	85.9	87.4
[16, 32, 48, 64]	366.7	15.1	77.5	86.1	87.4

* indicates a doubled number of experts in the second level of HoME layer.

Table 6: Segmentation performance on varying group sizes at each encoder stage.

Group size (K) ↓	Params (M) ↓	GPU (G) ↓	mDSC (%) ↑		
			PANORAMA	AMOS-CT	FeTA
[1024, 512, 256, 128]	170.5	13.1	77.2	86.1	87.4
[2048, 1024, 512, 256]	170.5	12.8	77.5	86.3	87.5
[2048, 1024, 512, 256]*	254.1	13.5	76.8	86.2	87.3
[4098, 2048, 1024, 512]	170.5	12.7	77.4	85.6	87.4

* indicates a doubled number of experts in the second level of HoME layer.

Table 7: Segmentation performance on varying number of slots per expert.

Slots (S) ↓	mDSC (%) ↑		
	PANORAMA	AMOS-CT	FeTA
1	76.2	85.9	87.3
2	77.2	86.0	87.4
4	77.5	86.3	87.5
8	76.5	86.1	87.4

Table 8: Qualitative comparison of Mamba-HoME trained with LayerNorm (LN) versus Dynamic Tanh (DyT).

Dataset	LN	DyT	mDSC (%) ↑
PANORAMA	✓	✗	77.4
	✗	✓	77.5
FETA	✓	✗	87.6
	✗	✓	87.7
AMOS-CT	✓	✗	87.4
	✗	✓	87.3
MVSeg	✓	✗	84.9
	✗	✓	85.0

²For this experiment, we use a patch size of $128 \times 128 \times 128$.

enabled by modality-agnostic feature representations. Pre-trained on CT and MRI scans, the model demonstrates superior adaptability to specialized tasks, such as fetal brain MRI segmentation in FeTA and 3D ultrasound mitral valve leaflets segmentation in MVSeg datasets.

This adaptability highlights the Mamba-HoME’s capacity to mitigate challenges posed by modality, resolution, and clinical context variations. Moreover, Mamba-HoME’s consistent high performance across heterogeneous datasets highlights its potential for practical deployment, where robust, modality-agnostic feature representations and precise segmentation are essential for scalable, real-world medical imaging solutions. As shown in Figure 3, supervised pre-training significantly improved Mamba-HoME’s performance compared to training from scratch and baseline, reducing artifacts and enhancing boundary segmentation for objects of varying sizes across three primary medical imaging modalities.

3.4 Generalizability analysis

To evaluate generalizability, we compare the proposed Mamba-HoME with several state-of-the-art networks. Specifically, we investigate four configurations along the AMOS dataset: (1) training solely on CT, (2) pre-training all models on CT and fine-tuning on MRI, (3) training solely on MRI, and (4) joint training on both CT and MRI. Table 2 shows that Mamba-HoME demonstrates superior generalizability across modalities compared to other models. Mamba-HoME, trained from scratch and further pre-trained on large-scale CT and MRI datasets, exhibits strong cross-modal generalizability to 3D ultrasound data, a modality with distinct challenges such as high noise and lower resolution. Leveraging robust, modality-agnostic feature representations, the pre-trained model adapts to 3D ultrasound via efficient fine-tuning, outperforming state-of-the-art methods in both DSC and boundary HD95 metrics, as shown in Table 4. Qualitative results in Figure 2 further illustrate its ability to handle ultrasound-specific artifacts. This cross-modal transferability highlights the model’s versatility across diverse imaging modalities. Moreover, Mamba-HoME shows a strong generalizability to external datasets within the same modality, especially MSD Pancreas and internal CT dataset for PDAC and pancreas segmentation, outperforms several state-of-the-art methods in both DSC and HD95 metrics (see Table 11).

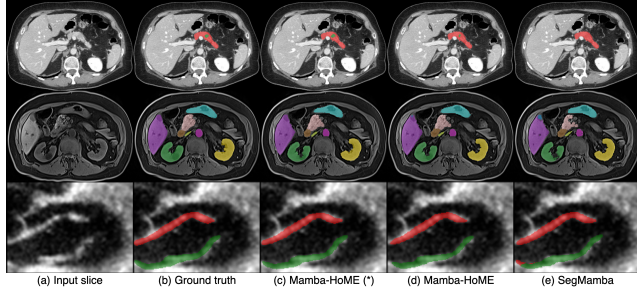


Figure 3: Qualitative comparison of Mamba-HoME fine-tuned, Mamba-HoME trained from scratch, and baseline SegMamba across PANORAMA (CT), AMOS-MRI (MRI), and MVSeg (3D US) for three modalities.

4 Conclusions

In this work, we introduce Hierarchical Soft Mixture-of-Experts (HoME), a two-level token-routing MoE layer designed to efficiently capture local-to-global pattern hierarchies. We integrate HoME with Mamba into the Mamba-HoME architecture, which enables long-sequence processing. Comprehensive experiments demonstrate that Mamba-HoME outperforms several state-of-the-art methods and generalizes well across the three primary 3D medical imaging modalities.

Limitations. Scalability to large-scale medical datasets (e.g., $>10,000$ scans) remains unexplored, limiting our understanding of Mamba-HoME’s generalization across diverse image distributions. Although the model is pre-trained on a large-scale multimodal dataset using supervised learning, its behavior under large-scale self-supervised learning (e.g., $>200,000$ scans) has not yet been studied. We identify this as a promising direction for future work to improve Mamba-HoME’s ability to capture complex patterns in unlabeled medical images.

References

- [1] Tugba Akinci D’Antonoli, Lucas K Berger, Ashraya K Indrakanti, Nathan Vishwanathan, Jakob Weiss, Matthias Jung, Zeynep Berkarda, Alexander Rau, Marco Reisert, Thomas Küstner, et al. Totalsegmentator mri: Robust sequence-independent segmentation of multiple anatomic structures in mri. *Radiology*, 314(2):e241613, 2025.
- [2] Nils Alves, Merlijn Schuurmans, Dominik Rutkowski, Derya Yakar, Ingfrid Haldorsen, Marjolein Liedenbaum, Anders Molven, Phillip Vendittelli, Geert Litjens, Jurgen Hermans, et al. The panorama study protocol: Pancreatic cancer diagnosis-radiologists meet ai. *Zenodo*, 2024.
- [3] Michela Antonelli, Annika Reinke, Spyridon Bakas, Keyvan Farahani, Annette Kopp-Schneider, Bennett A Landman, Geert Litjens, Bjoern Menze, Olaf Ronneberger, Ronald M Summers, et al. The medical segmentation decathlon. *Nature communications*, 13(1):4128, 2022.
- [4] Szymon Antoniak, Michał Krutul, Maciej Pióro, Jakub Krajewski, Jan Ludziejewski, Kamil Ciebiera, Krystian Król, Tomasz Odrzygóźdź, Marek Cygan, and Sebastian Jaszczur. Mixture of tokens: Continuous moe through cross-example aggregation. *Advances in Neural Information Processing Systems*, 37:103873–103896, 2024.
- [5] Anurag Arnab, Mostafa Dehghani, Georg Heigold, Chen Sun, Mario Lučić, and Cordelia Schmid. Vivit: A video vision transformer. In *Proceedings of the IEEE/CVF international conference on computer vision*, pages 6836–6846, 2021.
- [6] Reza Azad, Ehsan Khodapanah Aghdam, Amelie Rauland, Yiwei Jia, Atlas Haddadi Avval, Afshin Bozorgpour, Sanaz Karimijafarbigloo, Joseph Paul Cohen, Ehsan Adeli, and Dorit Merhof. Medical image segmentation review: The success of u-net. *IEEE Transactions on Pattern Analysis and Machine Intelligence*, 2024.
- [7] Jimmy Lei Ba, Jamie Ryan Kiros, and Geoffrey E Hinton. Layer normalization. *arXiv preprint arXiv:1607.06450*, 2016.
- [8] Hangbo Bao, Wenhui Wang, Li Dong, Qiang Liu, Owais Khan Mohammed, Kriti Aggarwal, Subhojit Som, Songhao Piao, and Furu Wei. Vlmo: Unified vision-language pre-training with mixture-of-modality-experts. *Advances in Neural Information Processing Systems*, 35:32897–32912, 2022.
- [9] Patrick Carnahan, John Moore, Daniel Bainbridge, Mehdi Eskandari, Elvis CS Chen, and Terry M Peters. Deepmitral: Fully automatic 3d echocardiography segmentation for patient specific mitral valve modelling. In *International Conference on Medical Image Computing and Computer-Assisted Intervention*, pages 459–468. Springer, 2021.
- [10] Ao Chang, Jiajun Zeng, Ruobing Huang, and Dong Ni. Em-net: Efficient channel and frequency learning with mamba for 3d medical image segmentation. In *International Conference on Medical Image Computing and Computer-Assisted Intervention*, pages 266–275. Springer, 2024.
- [11] Qian Chen, Lei Zhu, Hangzhou He, Xinliang Zhang, Shuang Zeng, Qiushi Ren, and Yanye Lu. Low-rank mixture-of-experts for continual medical image segmentation. In *International Conference on Medical Image Computing and Computer-Assisted Intervention*, pages 382–392. Springer, 2024.
- [12] Tianlong Chen, Xuxi Chen, Xianzhi Du, Abdullah Rashwan, Fan Yang, Huizhong Chen, Zhangyang Wang, and Yeqing Li. Adamv-moe: Adaptive multi-task vision mixture-of-experts. In *Proceedings of the IEEE/CVF International Conference on Computer Vision*, pages 17346–17357, 2023.
- [13] Tri Dao and Albert Gu. Transformers are ssms: generalized models and efficient algorithms through structured state space duality. In *Proceedings of the International Conference on Machine Learning*, pages 10041–10071, 2024.
- [14] Alexey Dosovitskiy, Lucas Beyer, Alexander Kolesnikov, Dirk Weissenborn, Xiaohua Zhai, Thomas Unterthiner, Mostafa Dehghani, Matthias Minderer, Georg Heigold, Sylvain Gelly, et al. An image is worth 16x16 words: Transformers for image recognition at scale. In *International Conference on Learning Representations*, 2021.
- [15] Zhiwen Fan, Rishov Sarkar, Ziyu Jiang, Tianlong Chen, Kai Zou, Yu Cheng, Cong Hao, Zhangyang Wang, et al. M³vit: Mixture-of-experts vision transformer for efficient multi-task learning with model-accelerator co-design. *Advances in Neural Information Processing Systems*, 35:28441–28457, 2022.
- [16] Yunhe Gao. Training like a medical resident: Context-prior learning toward universal medical image segmentation. In *Proceedings of the IEEE/CVF Conference on Computer Vision and Pattern Recognition*, pages 11194–11204, 2024.

- [17] Albert Gu and Tri Dao. Mamba: Linear-time sequence modeling with selective state spaces. *arXiv preprint arXiv:2312.00752*, 2023.
- [18] Xingru Huang, Jian Huang, Tianyun Zhang, HE HONG, Shaowei Jiang, Yaoqi Sun, et al. Upping the game: How 2d u-net skip connections flip 3d segmentation. *Advances in Neural Information Processing Systems*, 37:87282–87309, 2025.
- [19] Yuanfeng Ji, Haotian Bai, Chongjian Ge, Jie Yang, Ye Zhu, Ruimao Zhang, Zhen Li, Lingyan Zhanng, Wanling Ma, Xiang Wan, et al. Amos: A large-scale abdominal multi-organ benchmark for versatile medical image segmentation. *Advances in neural information processing systems*, 35:36722–36732, 2022.
- [20] Yufeng Jiang and Yiqing Shen. M4oe: A foundation model for medical multimodal image segmentation with mixture of experts. In *International Conference on Medical Image Computing and Computer-Assisted Intervention*, pages 621–631. Springer, 2024.
- [21] Jiachen Li, Xinyao Wang, Sijie Zhu, Chia-Wen Kuo, Lu Xu, Fan Chen, Jitesh Jain, Humphrey Shi, and Longyin Wen. Cumo: Scaling multimodal llm with co-upcycled mixture-of-experts. *Advances in Neural Information Processing Systems*, 37:131224–131246, 2024.
- [22] Wenxuan Li, Chongyu Qu, Xiaoxi Chen, Pedro RAS Bassi, Yijia Shi, Yuxiang Lai, Qian Yu, Huimin Xue, Yixiong Chen, Xiaorui Lin, et al. Abdomenatlas: A large-scale, detailed-annotated, & multi-center dataset for efficient transfer learning and open algorithmic benchmarking. *Medical Image Analysis*, 97:103285, 2024.
- [23] Wenxuan Li, Alan Yuille, and Zongwei Zhou. How well do supervised models transfer to 3d image segmentation? In *The Twelfth International Conference on Learning Representations*, 2024.
- [24] Jiarun Liu, Hao Yang, Hong-Yu Zhou, Lequan Yu, Yong Liang, Yizhou Yu, Shaoting Zhang, Hairong Zheng, and Shanshan Wang. Swin-umamba[†]: Adapting mamba-based vision foundation models for medical image segmentation. *IEEE Transactions on Medical Imaging*, 2024.
- [25] Tiange Liu, Qingze Bai, Drew A Torigian, Yubing Tong, and Jayaram K Udupa. Vsmtrans: A hybrid paradigm integrating self-attention and convolution for 3d medical image segmentation. *Medical image analysis*, 98:103295, 2024.
- [26] Ze Liu, Yutong Lin, Yue Cao, Han Hu, Yixuan Wei, Zheng Zhang, Stephen Lin, and Baining Guo. Swin transformer: Hierarchical vision transformer using shifted windows. In *Proceedings of the IEEE/CVF international conference on computer vision*, pages 10012–10022, 2021.
- [27] Ilya Loshchilov and Frank Hutter. Sgdr: Stochastic gradient descent with warm restarts. In *International Conference on Learning Representations*, 2017.
- [28] Basil Mustafa, Carlos Riquelme, Joan Puigcerver, Rodolphe Jenatton, and Neil Houlsby. Multimodal contrastive learning with limoe: the language-image mixture of experts. *Advances in Neural Information Processing Systems*, 35:9564–9576, 2022.
- [29] Adam Paszke, Sam Gross, Francisco Massa, Adam Lerer, James Bradbury, Gregory Chanan, Trevor Killeen, Zeming Lin, Natalia Gimeshein, Luca Antiga, et al. Pytorch: An imperative style, high-performance deep learning library. *Advances in neural information processing systems*, 32, 2019.
- [30] Kelly Payette, Hongwei Bran Li, Priscille de Dumast, Roxane Licandro, Hui Ji, Md Mahfuzur Rahman Siddiquee, Daguang Xu, Andriy Myronenko, Hao Liu, Yuchen Pei, et al. Fetal brain tissue annotation and segmentation challenge results. *Medical image analysis*, 88:102833, 2023.
- [31] Kelly Payette, Céline Steger, Roxane Licandro, Priscille De Dumast, Hongwei Bran Li, Matthew Barkovich, Liu Li, Maik Dannecker, Chen Chen, Cheng Ouyang, et al. Multi-center fetal brain tissue annotation (feta) challenge 2022 results. *IEEE Transactions on Medical Imaging*, 2024.
- [32] Szymon Plotka, Maciej Chrabaszcz, and Przemyslaw Biecek. Swin smt: Global sequential modeling for enhancing 3d medical image segmentation. In *International Conference on Medical Image Computing and Computer-Assisted Intervention*, pages 689–698. Springer, 2024.
- [33] Joan Puigcerver, Carlos Riquelme Ruiz, Basil Mustafa, and Neil Houlsby. From sparse to soft mixtures of experts. In *The Twelfth International Conference on Learning Representations*, 2024.
- [34] Chongyu Qu, Tiezheng Zhang, Hualin Qiao, Yucheng Tang, Alan L Yuille, Zongwei Zhou, et al. Abdomenatlas-8k: Annotating 8,000 ct volumes for multi-organ segmentation in three weeks. *Advances in Neural Information Processing Systems*, 36:36620–36636, 2023.

- [35] Carlos Riquelme, Joan Puigcerver, Basil Mustafa, Maxim Neumann, Rodolphe Jenatton, André Susano Pinto, Daniel Keysers, and Neil Houlsby. Scaling vision with sparse mixture of experts. *Advances in Neural Information Processing Systems*, 34:8583–8595, 2021.
- [36] Olaf Ronneberger, Philipp Fischer, and Thomas Brox. U-net: Convolutional networks for biomedical image segmentation. In *International Conference on Medical Image Computing and Computer-Assisted Intervention*, pages 234–241. Springer, 2015.
- [37] Holger R Roth, Le Lu, Amal Farag, Hoo-Chang Shin, Jiamin Liu, Evrim B Turkbey, and Ronald M Summers. Deeporgan: Multi-level deep convolutional networks for automated pancreas segmentation. In *International Conference on Medical Image Computing and Computer-Assisted Intervention*, pages 556–564. Springer, 2015.
- [38] Fenghe Tang, Bingkun Nian, Yingtai Li, Zihang Jiang, Jie Yang, Wei Liu, and S Kevin Zhou. Mambamim: Pre-training mamba with state space token interpolation and its application to medical image segmentation. *Medical Image Analysis*, page 103606, 2025.
- [39] Yucheng Tang, Dong Yang, Wenqi Li, Holger R Roth, Bennett Landman, Daguang Xu, Vishwesh Nath, and Ali Hatamizadeh. Self-supervised pre-training of swin transformers for 3d medical image analysis. In *Proceedings of the IEEE/CVF conference on computer vision and pattern recognition*, pages 20730–20740, 2022.
- [40] Guoan Wang, Jin Ye, Junlong Cheng, Tianbin Li, Zhaolin Chen, Jianfei Cai, Junjun He, and Bohan Zhuang. Sam-med3d-moe: Towards a non-forgetting segment anything model via mixture of experts for 3d medical image segmentation. In *International Conference on Medical Image Computing and Computer-Assisted Intervention*, pages 552–561. Springer, 2024.
- [41] Hualiang Wang, Yiqun Lin, Xinpeng Ding, and Xiaomeng Li. Tri-plane mamba: Efficiently adapting segment anything model for 3d medical images. In *International Conference on Medical Image Computing and Computer-Assisted Intervention*, pages 636–646. Springer, 2024.
- [42] Boqian Wu, Qiao Xiao, Shiwei Liu, Lu Yin, Mykola Pechenizkiy, Decebal Constantin Mocanu, Maurice Keulen, and Elena Mocanu. E2enet: Dynamic sparse feature fusion for accurate and efficient 3d medical image segmentation. *Advances in Neural Information Processing Systems*, 37:118483–118512, 2025.
- [43] Linshan Wu, Jiaxin Zhuang, and Hao Chen. Voco: A simple-yet-effective volume contrastive learning framework for 3d medical image analysis. In *Proceedings of the IEEE/CVF Conference on Computer Vision and Pattern Recognition*, pages 22873–22882, 2024.
- [44] Zhaohu Xing, Tian Ye, Yijun Yang, Guang Liu, and Lei Zhu. Segmamba: Long-range sequential modeling mamba for 3d medical image segmentation. In *International Conference on Medical Image Computing and Computer-Assisted Intervention*, pages 578–588. Springer, 2024.
- [45] Zeyue Xue, Guanglu Song, Qiushan Guo, Boxiao Liu, Zhuofan Zong, Yu Liu, and Ping Luo. Raphael: Text-to-image generation via large mixture of diffusion paths. *Advances in Neural Information Processing Systems*, 36:41693–41706, 2023.
- [46] Yanqi Zhou, Tao Lei, Hanxiao Liu, Nan Du, Yanping Huang, Vincent Zhao, Andrew M Dai, Quoc V Le, James Laudon, et al. Mixture-of-experts with expert choice routing. *Advances in Neural Information Processing Systems*, 35:7103–7114, 2022.
- [47] Zongwei Zhou, Md Mahfuzur Rahman Siddiquee, Nima Tajbakhsh, and Jianming Liang. Unet++: Redesigning skip connections to exploit multiscale features in image segmentation. *IEEE Transactions on Medical Imaging*, 39(6):1856–1867, 2019.
- [48] Jiachen Zhu, Xinlei Chen, Kaiming He, Yann LeCun, and Zhuang Liu. Transformers without normalization. In *Proceedings of the IEEE/CVF Conference on Computer Vision and Pattern Recognition*, 2025.
- [49] Xingkui Zhu, Yiran Guan, Dingkan Liang, Yuchao Chen, Yuliang Liu, and Xiang Bai. Moe jetpack: From dense checkpoints to adaptive mixture of experts for vision tasks. *Advances in Neural Information Processing Systems*, 37:12094–12118, 2024.

A Datasets

Table 9 shows an overview of the datasets used for pre-training, training and testing.

Table 9: An overview of the datasets used for pre-training, training, and testing. These datasets, spanning two modalities (CT and MRI), cover diverse anatomical structures and lesions.

No.	Dataset	Modality	Body part	Mode	Label type	Pre-training	Train	Test
1.	AbdomenAtlas1.1 [34, 22]	CT	Abdomen	Pre-training	Voxel-wise	8,788 (-474)	-	-
2.	TotalSegmentator MRI [1]	MRI	Whole-body	Pre-training	Voxel-wise	616	-	-
3.	PANORAMA [2]	CT	Abdomen	Fine-tuning	Voxel-wise	-	1,964	334
4.	AMOS 2022 [19]	CT-MRO	Abdomen	Fine-tuning	Voxel-wise	-	240	120
5.	FeTA 2022 [31]	MRI	Fetal brain	Fine-tuning	Voxel-wise	-	120	-
6.	MVSeg2023 [9]	US	Heart	Fine-tuning	Voxel-wise	-	110	-
7.	In-house CT	CT	Abdomen	Test	Voxel-wise	-	-	60
Total						9,404	2,434	514

A.1 Pre-training

For pre-training, we utilize two publicly available datasets with two modalities: AbdomenAtlas 1.1 [22, 34, 23, 22], which includes CT scans, and TotalSegmentator [1], which includes MRI scans.

AbdomenAtlas. For pre-training, we use the AbdomenAtlas 1.1 dataset³, which consists of 9,262 CT scans with manually voxel-wise annotated 25 anatomical structures. The dataset consists of mix of non-contrast, arterial, portal-venous, and delayed phases. Each CT image consists of 24~2,572 slices, with a resolution ranging from 188×79 to 971×651 pixels. The voxel spatial resolution ranges $([0.38 \sim 1.5] \times [0.38 \sim 3.0] \times [0.3 \sim 8.0])\text{mm}^3$ with a mean of $0.84 \times 0.84 \times 2.4 \text{ mm}^3$. From AbdomenAtlas 1.1, we excluded overlap cases from the PANORAMA dataset, including 194 MSD Pancreas cases and 43 NIH Pancreas cases, and 200 training cases from the AMOS2022 CT dataset.

TotalSegmentator MRI. The TotalSegmentator MRI dataset consists of 616 MRI images with 50 anatomical structures manually annotated at the voxel level. For pre-training, we select 22 classes that match those in the AbdomenAtlas dataset. Each MRI scan consists of 5~1,915 slices. The voxel spatial resolution ranges $([0.17 \sim 20.0] \times [0.17 \sim 25.0] \times [0.17 \sim 28.0])\text{mm}^3$ with a mean of $1.28 \times 1.86 \times 2.81 \text{ mm}^3$. Table 10 shows the class map from both modalities used for pre-training the model.

Table 10: Class mapping for anatomical structures in CT scans (AbdomenAtlas) and MRI scans (TotalSegmentator MRI).

Index	Class	Index	Class
0	Background	13	Celiac trunk
1	Aorta	14	Colon
2	Gall bladder	15	Duodenum
3	Kidney (left)	16	Esophagus
4	Kidney (right)	17	Femur (left)
5	Liver	18	Femur (right)
6	Pancreas	19	Hepatic vessel
7	Postcava	20	Intestine
8	Spleen	21	Lung (left)
9	Stomach	22	Lung (right)
10	Adrenal gland (left)	23	Portal vein & splenic vein
11	Adrenal gland (right)	24	Prostate
12	Bladder	25	Rectum

³Please note that, for a fair comparison, we excluded 200 cases from AMOS, 194 from Pancreas-MSD, and 80 from NIH, respectively. These scans correspond to the original AMOS dataset and partly to the PANORAMA dataset.

A.2 Training, fine-tuning, and test

To validate the efficiency of the Mamba-HoME, we conduct comprehensive experiments on both publicly and in-house available datasets across three primary modalities. For CT, we use PANORAMA [2], AMOS2022 CT [19], and a private data set for segmentation and diagnosis of pancreatic ductal adenocarcinoma (PDAC) in abdominal CT. For MRI, we use AMOS2022 MRI [19], and FeTA 2022, which includes brain fetal MRI [30, 31]. For US, we use MVSeg2023 [9].

PANORAMA. The PANORAMA dataset [2] comprises 2,238 multi-center contrast-enhanced computed tomography (CECT) scans acquired in a single portal-venous phase. It includes 1,964 newly acquired scans from five European centers, as well as publicly available data from two medical datasets in the United States, namely NIH [37] and MSD Pancreas [3]. The dataset consists 676 PDAC (pancreatic ductal adenocarcinoma), and 1,562 non-PDAC cases, respectively. While the dataset contains six voxel-wise labels, PDAC lesion, veins, arteries, pancreatic parenchyma, pancreatic duct, and common bile duct, we use only the PDAC lesion and merge the pancreatic parenchyma and pancreatic duct classes into a single *pancreas* label. Each CT image consists of 37~1,572 slices, with a resolution ranging from 512×512 to 1024×1024 pixels. The voxel spatial resolution ranges $([0.31 \sim 1.03] \times [0.31 \sim 1.03] \times [0.45 \sim 5.0])\text{mm}^3$ with a mean of $0.75 \times 0.75 \times 2.0 \text{ mm}^3$.

AMOS 2022. The dataset consists of 600 scans in total (500 CT and 100 MRI). However, the ground truth is available only for the training and validation set, which consists of 240, and 120 scans, respectively. Each scan consists of 15 anatomical structures, manually annotated at the voxel level. For a training, and evaluation of AMOS-CT, we use 200, and 100 scans for training and test, respectively. For a training, and evaluation of AMOS-MRI, we use 40, and 20 scans for training and test, respectively. The median spacing for used CT scans (training, and test sets) is $0.68 \times 0.68 \times 5.0 \text{ mm}^3$.

FeTA 2022. The dataset comprises 120 cases of MRI scans for fetal brain tissue segmentation, collected from two prominent medical centers: the University Children’s Hospital Zurich and the Medical University of Vienna. The dataset includes 80 cases from Zurich and 40 from Vienna. It features seven manually annotated tissues, with voxel-wise annotations provided for each: external cerebrospinal fluid, gray matter, white matter, ventricles, cerebellum, deep gray matter, and the brainstem. The MRI data from Zurich and Vienna were acquired at isotropic resolutions of $0.5 \times 0.5 \times 0.5 \text{ mm}^3$ and $1 \times 1 \times 1 \text{ mm}^3$, respectively.

MVSeg 2023. The dataset [9] consists of 175 transesophageal echocardiography(TEE) 3D US scans for mitral valve segmentation. Each scan consists voxel-wise annotations provided for the posterior leaflet, and the anterior leaflet. Data was acquired at King’s College Hospital, London, UK.

In-house CT. 60 CECT scans of histopathology-confirmed PDAC cases, acquired from 40 medical centers, each containing 68~875 slices with a voxel spatial resolution ranging $([0.47 \sim 0.98] \times [0.47 \sim 0.98] \times [0.5 \sim 5.0])\text{mm}^3$. These scans contain voxel-wise annotations of both the pancreas and the PDAC. The diameter size of the PDAC ranges 1.25~6.06 cm, with a mean of $3.45 \pm 1.20 \text{ cm}$. All test CECT scans have a resolution of 512×512 pixels. Two junior radiologists annotated the in-house data using 3D Slicer, which was reviewed by two domain experts with more than 30 years of experience.

B Experimental setup

All training utilizes the \mathcal{L}_{DiceCE} loss function with the AdamW optimizer, an initial learning rate of $1e^{-4}$ with a cosine annealing scheduler [27], a weight decay of $1e^{-5}$, and a batch size of 2.

To improve gradient stability and computational efficiency in SSMs, we use Dynamic Tanh (DyT) [48] normalization, defined as:

$$f_{\text{DyT}}(x) = w \cdot \tanh(\alpha \cdot x) + b, \quad (13)$$

where $x \in \mathbb{R}^{B \times d}$ is the input tensor, $w, b \in \mathbb{R}^d$ are learnable per-channel vector parameters, and $\alpha \in \mathbb{R}$ is a shared scalar. DyT applies a point-wise nonlinearity, leveraging the bounded nature of \tanh to stabilize gradients. Unlike LayerNorm [7], it avoids costly mean and variance computations, reducing overhead while maintaining $\mathcal{O}(Bd)$ complexity. DyT accelerates training and validation with performance on par with normalization-based alternatives.

The experiments are conducted on a workstation equipped with $8 \times$ NVIDIA H100 GPUs. For implementation, we employ Python 3.11, PyTorch 2.4 [29], and MONAI 1.3.0 within a Distributed Data-Parallel (DDP) training setup.

B.1 Pre-training

AbdomenAtlas and TotalSegmentator MRI. Each CT and MRI scans are resampled into a spacing of $0.8 \times 0.8 \times 3.0 \text{ mm}^3$ resolution. Before training, we randomly split the data in an 85:15 ratio, ensuring a consistent number of CT and MRI scans in both the training and validation sets. All CT scans are clipped to the window of the Hounsfield Unit of $[-175, 250]$, while MRI scans are clipped to $[0, 1000]$. Both modalities are linearly scaled to $[0, 1]$. We train Mamba-HoME with a patch size of $96 \times 96 \times 96$ for 800 epochs. During the inference stage, we use a sliding-window algorithm with a patch size of $96 \times 96 \times 96$ and an overall of 0.5 with a Gaussian filter. The pre-training took around 7 days.

B.2 Training and Fine-tuning

PANORAMA. Each CT scan is resampled into the spacing of $0.8 \times 0.8 \times 3 \text{ mm}^3$ resolution. All CT scans are clipped to the window of the Hounsfield Unit of $[-175, 250]$ and linearly scaled to $[0, 1]$. During training, we randomly select 1,571 scans (80%) for training and 393 scans (20%) for validation sets, maintaining the distribution ratio of PDAC to non-PDAC cases. During the inference stage, we use a sliding-window algorithm with a patch size of $192 \times 192 \times 48$ and an overlap of 0.5 with a Gaussian filter. We train the model for 500 epochs.

AMOS-CT and AMOS-MRI. We resample each CT and MRI scan to the $1.5 \times 1.5 \times 1.5 \text{ mm}^3$ isotropic resolution. All CT scans are clipped to the window of the Hounsfield Unit of $[-175, 250]$, while MRI scans are clipped to $[0, 1000]$. Both modalities are linearly scaled to $[0, 1]$. We randomly split an original training dataset into train and validation subsets with 80:20 ratio. During the training, we crop random patches of $128 \times 128 \times 128$, and a sliding window algorithm with a default overlap of 0.5 is performed for validation. During training, we employ on-the-fly augmentations, including scaling, rotation, flipping, adjusting brightness and contrast, and Gaussian smoothness and noise.

FeTA 2022. We resample each MRI volume into $0.8 \times 0.8 \times 0.8 \text{ mm}^3$ isotropic resolution. We clip each MRI scan value of $[0, 1000]$ and linearly scale to $[0, 1]$. We train the models using a five-fold cross-validation strategy for 300 epochs each. During training, we crop random patches of $128 \times 128 \times 128$, and we employ on-the-fly augmentations, including scaling, rotation, flipping, adjusting brightness and contrast, Gaussian smoothness and noise, and affine transformations.

MVSeg 2023. We resample each US scan into $0.5 \times 0.5 \times 0.5 \text{ mm}^3$ isotropic resolution. We clip each US scan value of $[0, 255]$ and linearly scale to $[0, 1]$. We train the models using an original train, valid, and test split, including 105, 30, and 40 scans, respectively. We use 500 epochs for each training. During training, we crop random patches of $128 \times 128 \times 128$, and we employ on-the-fly augmentations, including scaling, rotation, flipping, adjusting brightness and contrast, Gaussian smoothness and noise, and affine transformations.

B.3 Evaluation metrics

Dice Similarity Coefficient (DSC). The DSC is a commonly used metric to evaluate the segmentation performance of a model in multi-class settings, especially in medical imaging. It measures the overlap between predicted and ground truth segmentations, providing an aggregate assessment across multiple classes. Given a segmentation task with C classes, let $\mathbf{p}_i \in \mathbb{R}^C$ and $\mathbf{g}_i \in \mathbb{R}^C$ be the one-hot encoded predicted and ground truth vectors at voxel i , respectively. The DSC for class c is computed as:

$$DSC_c = \frac{2 \sum_i p_{i,c} g_{i,c}}{\sum_i p_{i,c} + \sum_i g_{i,c}} \quad (14)$$

where $p_{i,c}$ and $g_{i,c}$ represent the predicted and ground truth binary masks for class c at voxel i , respectively. The mean DSC (mDSC) across all C classes is computed as:

$$\text{mDSC} = \frac{1}{C} \sum_{c=1}^C \text{DSC}_c \quad (15)$$

This metric ensures that each class contributes equally to the final score, regardless of class imbalance.

95th percentile Hausdorff Distance (HD95). The HD95 is a commonly used metric to evaluate the spatial similarity between predicted and ground truth segmentations. It measures the worst-case boundary discrepancy between two sets but is made more robust by considering the 95th percentile instead of the maximum distance. Given a segmentation task with C classes, let S_c^P and S_c^G denote the sets of boundary points for the predicted and ground truth segmentations for class c , respectively. The directed Hausdorff distance from S_c^P to S_c^G is defined as:

$$d_H(S_c^P, S_c^G) = \max_{p \in S_c^P} \min_{g \in S_c^G} \|p - g\|_2, \quad (16)$$

where $\|p - g\|_2$ denotes the Euclidean distance between points p and g . The bi-directional Hausdorff distance is given by:

$$d_H(S_c^P, S_c^G) = \max \left(\max_{p \in S_c^P} \min_{g \in S_c^G} \|p - g\|_2, \max_{g \in S_c^G} \min_{p \in S_c^P} \|g - p\|_2 \right). \quad (17)$$

Instead of using the maximum, the 95th percentile Hausdorff distance is computed to mitigate the influence of outliers:

$$\text{HD95}_c = \text{percentile}_{95} (\{d_H(S_c^P, S_c^G), d_H(S_c^G, S_c^P)\}). \quad (18)$$

The mean HD95 (mHD95) across all classes is then given by:

$$\text{mHD95} = \frac{1}{C} \sum_{c=1}^C \text{HD95}_c \quad (19)$$

This metric is widely used in medical image segmentation to quantify boundary errors while reducing the sensitivity to small outlier deviations.

Sensitivity and Specificity. The sensitivity and specificity are crucial metrics for evaluating the performance of a model in detecting the presence of a condition at the patient level. In this setting, a segmentation model processes medical scans and outputs a binary classification for each patient: either *positive* (presence of the condition) or *negative* (absence of the condition).

Given a dataset of patients, let TP , FP , FN , and TN denote the number of true positives, false positives, false negatives, and true negatives, respectively. The sensitivity (also known as recall or true positive rate) is defined as:

$$\text{Sensitivity} = \frac{TP}{TP + FN}, \quad (20)$$

where sensitivity measures the proportion of correctly identified positive patients out of all actual positive patients. The specificity (true negative rate) is given by:

$$\text{Specificity} = \frac{TN}{TN + FP}, \quad (21)$$

where specificity quantifies the proportion of correctly identified negative patients out of all actual negative patients.

These metrics provide a comprehensive assessment of the model's ability to detect the condition while avoiding false alarms, which is critical for clinical decision-making.

Number of parameters. The total number of trainable parameters in a neural network can be computed by summing the parameters across all layers and levels, as follows:

$$\text{Parameters} = \|\Theta\|_0 + \sum_{l=1}^L \sum_{k=1}^{L-l} \sum_{i=1}^{C_l} \sum_{j=1}^{C_k} A_{l,k}^{i,j} \|\theta_{l,k}^{i,j}\|_0, \quad (22)$$

where: Θ represents the set of parameters from the backbone, L is the total number of levels or layers in the network, C_l and C_k represent the number of input and output channels at each level l and k , respectively, $A_{l,k}^{i,j}$ is a binary matrix indicating the presence of a weight connection between input channel i at level l and output channel j at level k , $\|\theta_{l,k}^{i,j}\|_0$ represents the count of non-zero weights in the connection between input channel i and output channel j .

This formulation takes into account the layer-wise parameters while incorporating the structured sparsity of weights within the network.

C Additional experimental results

Table 11: Quantitative results on PANORAMA test sets, including NIH, MSD Pancreas, and one in-house set. We report mDSC (%) and mHD95 (mm) for the pancreas and PDAC. Please note, NIH dataset consists only of healthy controls. Patient-level PDAC detection is evaluated using sensitivity (%) and specificity (%). The best results are **bolded**, while the second-best are underlined. (*) denotes pre-trained model. Please note, SuPreM was partially pre-trained on a subset of the test set, including the Pancreas MSD and NIH datasets, which may result in an unfair comparison.

Method	Segmentation (mDSC %) \uparrow							Segmentation (mHD95 mm) \downarrow		PDAC Detection \uparrow		
	NIH		MSD Pancreas		In-house		Overall		Overall		Overall (%)	
	Pancreas	PDAC	Pancreas	PDAC	Pancreas	PDAC	Pancreas	Pancreas	PDAC	Sensitivity	Specificity	
VoCo-B (*)	90.1 \pm 5.0	38.7 \pm 28.9	86.5 \pm 7.2	43.3 \pm 24.1	80.3 \pm 11.7	40.5 \pm 27.2	86.3 \pm 8.4	3.0 \pm 4.8	271.5 \pm 144.2	86.1	91.6	
Hermes	92.0 \pm 2.8	40.0 \pm 32.8	86.5 \pm 8.9	58.3 \pm 25.6	80.8 \pm 11.3	48.2 \pm 30.6	87.8 \pm 8.0	2.7 \pm 4.9	23.9 \pm 60.5	87.3	94.0	
Swin SMT	91.9 \pm 2.8	44.0 \pm 32.6	87.2 \pm 6.0	58.6 \pm 24.2	79.8 \pm 11.0	49.4 \pm 30.6	87.0 \pm 7.8	4.8 \pm 23.9	92.1 \pm 124.7	88.6	92.8	
VSmTrans	92.0 \pm 2.4	47.1 \pm 30.6	87.3 \pm 6.5	56.1 \pm 26.9	80.5 \pm 11.4	50.3 \pm 29.6	87.2 \pm 7.9	3.5 \pm 15.8	82.1 \pm 65.4	89.9	90.4	
SegMamba	<u>92.7\pm2.6</u>	47.9 \pm 32.5	<u>88.8\pm6.4</u>	54.0 \pm 29.6	81.9 \pm 10.5	49.7 \pm 31.5	88.5\pm7.6	4.3 \pm 22.1	36.3 \pm 94.7	84.8	95.2	
uC 3DU-Net	92.6 \pm 2.6	49.0 \pm 31.2	88.9\pm6.7	56.8 \pm 26.5	80.2 \pm 11.8	52.0 \pm 29.7	88.2 \pm 8.3	2.9 \pm 4.1	18.2 \pm 21.0	80.7	89.2	
Swin UNETR	91.9 \pm 2.1	38.8 \pm 28.8	87.4 \pm 5.7	58.7 \pm 23.3	81.3 \pm 9.8	46.3 \pm 28.5	87.4 \pm 7.0	5.9 \pm 25.0	187.1 \pm 112.3	87.3	90.4	
SuPreM (*)	92.3 \pm 2.7	46.0 \pm 33.3	88.6 \pm 5.1	<u>61.4\pm24.0</u>	<u>82.0\pm10.2</u>	51.7 \pm 31.2	88.3 \pm 6.8	2.4 \pm 4.3	9.0 \pm 13.0	87.3	89.2	
Mamba-HoME	92.9\pm2.2	<u>51.2\pm30.5</u>	88.4 \pm 7.0	60.8 \pm 26.8	81.7 \pm 11.2	<u>54.8\pm29.5</u>	<u>88.3\pm8.1</u>	<u>2.3\pm4.2</u>	<u>8.4\pm12.1</u>	<u>90.4</u>	92.8	
Mamba-HoME (*)	92.6 \pm 2.4	53.6\pm31.9	88.5 \pm 6.8	61.7\pm25.7	82.3\pm10.3	56.7\pm29.9	88.5\pm7.6	1.9\pm3.1	6.2\pm10.2	92.8	95.2	

Table 12: Qualitative results on AMOS2022 CT validation set. We report mDSC (%) and HD95 (mm) for each organ across all folds. Organs include Spleen (Sp), Right Kidney (RK), Left Kidney (LK), Gallbladder (GB), Esophagus (Es), Liver (Li), Stomach (St), Aorta (Ao), Inferior Vena Cava (IVC), Pancreas (Pa), Right Adrenal Gland (RAG), Left Adrenal Gland (LAG), Duodenum (Du), Bladder (Bl), and Prostate/Uterus (Pr/Ut). The best results are **bolded**, while the second-best are underlined. (*) indicates pre-trained model.

Method	DSC (%) \uparrow								
	Sp	RK	LK	GB	Es	Li	St	Ao	IVC
Hermes	95.7 \pm 2.3	94.5 \pm 4.4	95.3 \pm 2.2	80.9 \pm 19.5	81.1 \pm 11.0	93.9 \pm 9.5	88.0 \pm 14.6	92.9 \pm 4.1	87.8 \pm 5.6
Swin SMT	95.4 \pm 5.4	95.6\pm1.8	95.1 \pm 2.5	76.3 \pm 24.0	81.3 \pm 10.1	92.2 \pm 12.8	87.4 \pm 14.3	<u>93.7\pm3.5</u>	88.6 \pm 4.4
VSmTrans	95.6 \pm 2.5	94.7 \pm 3.1	94.5 \pm 3.2	82.7 \pm 17.1	76.4 \pm 12.0	95.2 \pm 4.1	86.9 \pm 13.6	<u>92.9\pm4.8</u>	83.1 \pm 10.8
SegMamba	95.7 \pm 3.3	95.5 \pm 1.9	95.2 \pm 2.9	81.7 \pm 18.8	81.1 \pm 10.3	94.9 \pm 6.2	87.7 \pm 15.1	93.2 \pm 4.1	88.8 \pm 3.8
uC 3DU-Net	93.0 \pm 8.8	94.6 \pm 3.2	94.3 \pm 5.2	73.6 \pm 24.3	78.8 \pm 12.3	93.4 \pm 9.6	82.5 \pm 17.2	92.4 \pm 4.3	85.5 \pm 6.3
Swin UNETR	95.2 \pm 4.8	95.1 \pm 2.6	94.5 \pm 4.3	72.2 \pm 27.8	80.4 \pm 12.2	90.2 \pm 15.2	81.0 \pm 22.6	93.2 \pm 4.1	87.9 \pm 5.1
SuPreM (*)	95.6 \pm 2.7	95.0 \pm 1.7	94.4 \pm 5.0	86.2\pm12.0	79.4 \pm 9.7	97.1\pm1.2	91.2 \pm 9.4	93.0 \pm 3.2	88.7 \pm 4.0
Mamba-HoME	96.0\pm2.5	95.0 \pm 4.2	94.4 \pm 4.1	81.7 \pm 19.9	<u>82.0\pm10.2</u>	94.7 \pm 7.9	<u>90.2\pm13.1</u>	93.8\pm3.0	88.9\pm4.0
Mamba-HoME (*)	96.0\pm2.5	95.4 \pm 1.8	95.4\pm2.2	<u>85.3\pm15.5</u>	82.1\pm9.5	<u>96.8\pm1.7</u>	91.3\pm10.2	93.3 \pm 4.0	88.6 \pm 4.3

Method	DSC (%) \uparrow						mDSC (%) \uparrow	mHD95 (mm) \downarrow
	Pa	RAG	LAG	Du	Bl	Pr/Ut		
Hermes	82.5 \pm 12.2	73.7 \pm 13.1	71.8 \pm 15.4	77.7 \pm 14.4	83.3 \pm 19.9	79.3 \pm 17.3	85.3 \pm 14.7	40.5 \pm 87.2
Swin SMT	84.1 \pm 10.1	74.4 \pm 12.2	73.4 \pm 13.3	78.3 \pm 13.5	86.6 \pm 17.1	82.6 \pm 14.8	85.7 \pm 14.3	91.4 \pm 153.2
VSmTrans	84.0 \pm 10.0	72.9 \pm 11.2	74.7\pm12.0	77.8 \pm 12.7	<u>86.8\pm15.6</u>	81.6 \pm 16.2	85.3 \pm 13.4	178.7 \pm 190.5
SegMamba	84.0 \pm 10.0	74.7\pm11.4	74.0 \pm 12.7	77.3 \pm 14.1	83.9 \pm 17.5	82.6 \pm 12.5	86.0 \pm 13.3	98.9 \pm 138.9
uC 3DU-Net	75.4 \pm 16.0	73.3 \pm 11.3	71.1 \pm 14.6	69.8 \pm 17.0	83.0 \pm 17.1	79.1 \pm 15.6	82.7 \pm 16.0	47.3 \pm 91.7
Swin UNETR	81.6 \pm 13.1	74.4 \pm 11.5	74.5 \pm 11.5	78.1 \pm 13.6	85.0 \pm 16.5	80.8 \pm 13.8	84.3 \pm 15.7	94.7 \pm 156.2
SuPreM (*)	85.3\pm8.8	69.3 \pm 10.0	68.8 \pm 11.5	81.3\pm8.6	86.0 \pm 15.1	78.9 \pm 15.4	86.0 \pm 12.6	66.0 \pm 100.2
Mamba-HoME	84.0 \pm 10.8	74.4 \pm 11.3	74.1 \pm 13.1	78.4 \pm 13.5	83.8 \pm 18.7	83.2\pm14.9	<u>86.3\pm13.5</u>	45.0 \pm 85.1
Mamba-HoME (*)	<u>84.7\pm10.1</u>	74.0 \pm 11.7	<u>74.6\pm11.8</u>	<u>80.8\pm11.4</u>	88.0\pm13.8	<u>82.8\pm15.5</u>	87.3\pm12.1	32.0\pm64.2

Table 13: Quantitative results of 5-fold cross-validation on the FeTA 2022 dataset. We report the mDSC (%) and HD95 (mm) for each class and across all folds. Results are provided for external cerebrospinal fluid (eCSF), gray matter (GM), white matter (WM), ventricles (V), cerebellum (C), deep gray matter (dGM), and brainstem (B). The best results are **bolded**, while the second-best are underlined. (*) indicates pre-trained model.

Method	DSC (%) \uparrow							mDSC (%) \uparrow	HD95 (mm) \downarrow
	eCSF	GM	WM	V	C	dGM	B		
VoCo-B (*)	78.9 \pm 6.2	73.4 \pm 3.1	90.2 \pm 1.8	87.5 \pm 1.2	87.0 \pm 2.9	87.6 \pm 1.6	83.8 \pm 2.6	86.0 \pm 1.8	4.0 \pm 3.2
Swin SMT	78.3 \pm 5.7	72.6 \pm 2.8	90.0 \pm 1.8	86.2 \pm 2.3	86.6 \pm 1.1	87.9 \pm 1.9	83.8 \pm 2.0	85.6 \pm 1.3	2.4 \pm 0.3
Hermes	79.3 \pm 6.0	74.2 \pm 2.8	90.7 \pm 1.4	87.6 \pm 1.3	87.1 \pm 2.3	<u>88.8\pm1.8</u>	84.7 \pm 2.4	86.5 \pm 1.5	4.0 \pm 3.4
SegMamba	79.6 \pm 5.7	73.7 \pm 3.1	90.6 \pm 1.5	87.1 \pm 1.7	87.5 \pm 1.9	<u>88.8\pm1.6</u>	85.2 \pm 1.9	86.5 \pm 1.2	5.8 \pm 1.9
uC 3DU-Net	79.1 \pm 6.1	73.2 \pm 2.9	90.3 \pm 1.5	87.4 \pm 1.2	86.0 \pm 2.8	88.0 \pm 1.8	83.4 \pm 2.6	85.9 \pm 1.7	3.5 \pm 2.1
SuPreM (*)	78.0 \pm 6.1	71.7 \pm 3.4	89.8 \pm 1.7	86.8 \pm 1.8	85.9 \pm 3.6	87.1 \pm 1.4	83.5 \pm 2.7	85.3 \pm 1.8	3.6 \pm 2.3
VSmTrans	79.0 \pm 5.7	73.1 \pm 3.1	90.6 \pm 1.5	87.2 \pm 1.7	87.2 \pm 0.9	88.3 \pm 1.7	84.2 \pm 2.1	86.1 \pm 1.2	2.3 \pm 0.3
Mamba-HoME	80.4 \pm 5.8	<u>75.3\pm3.1</u>	<u>91.2\pm1.5</u>	<u>88.2\pm1.3</u>	<u>88.8\pm1.7</u>	89.4\pm1.8	86.6\pm1.5	<u>87.5\pm1.2</u>	<u>2.1\pm0.2</u>
Mamba-HoME (*)	80.6\pm4.3	76.1\pm2.6	91.9\pm1.1	88.8\pm0.8	90.0\pm0.9	<u>88.8\pm1.9</u>	<u>86.1\pm1.2</u>	87.7\pm1.0	2.0\pm0.2

Table 14: Quantitative results on MVSeg2023 test set. We report mDSC (%) and HD95 (mm) for the posterior leaflet and the anterior leaflet on the MVSeg2023 test set. The best results are **bolded**, while the second-best are underlined. (*) indicates pre-trained model.

Method	DSC (%) \uparrow		mDSC (%) \uparrow	HD95 (mm) \downarrow
	Posterior leaflet	Anterior leaflet		
Swin SMT	82.2 \pm 8.2	84.5 \pm 4.7	83.4 \pm 6.8	17.2 \pm 21.9
Hermes	82.9 \pm 6.8	84.1 \pm 5.5	83.5 \pm 6.2	13.3 \pm 13.8
uC 3DU-Net	82.9 \pm 6.8	85.0 \pm 4.3	83.9 \pm 5.8	13.4 \pm 15.7
SuPreM	83.2 \pm 7.6	85.4 \pm 4.7	84.3 \pm 6.4	12.9 \pm 14.6
VoCo-B	83.3 \pm 7.3	85.3 \pm 3.9	84.3 \pm 5.9	17.2 \pm 22.0
Swin UNETR	83.8 \pm 5.9	85.1 \pm 4.6	84.4 \pm 5.3	13.1 \pm 12.3
SegMamba	83.0 \pm 5.8	84.7 \pm 4.1	83.8 \pm 5.1	15.6 \pm 16.4
VSmTrans	83.4 \pm 6.5	85.4 \pm 3.7	84.4 \pm 5.5	17.4 \pm 24.4
Mamba-HoME	84.0 \pm 5.8	85.7 \pm 3.8	84.8 \pm 5.1	12.6 \pm 12.6
Mamba-HoME (*)	84.2\pm5.8	86.0\pm3.7	85.0\pm4.9	12.2\pm12.3

D Generalizability analysis

Figure 4 showcases the general overview of the Mamba-HoME framework with ground truth voxel-wise labels across cross-modal and cross-anatomical domains. The framework, initially developed using a combination of CT and MRI scans, presents consistent ground truth segmentations of abdominal organs such as the liver, spleen, and kidneys across multiple columns. Furthermore, the inclusion of Fetal MRI for fine-tuning highlights its ability to represent distinct anatomical features in fetal imaging, despite the differences from standard MRI exams. This cross-modal and cross-anatomical representation underscores the Mamba-HoME network versatility in capturing variations in imaging techniques and anatomical structures.

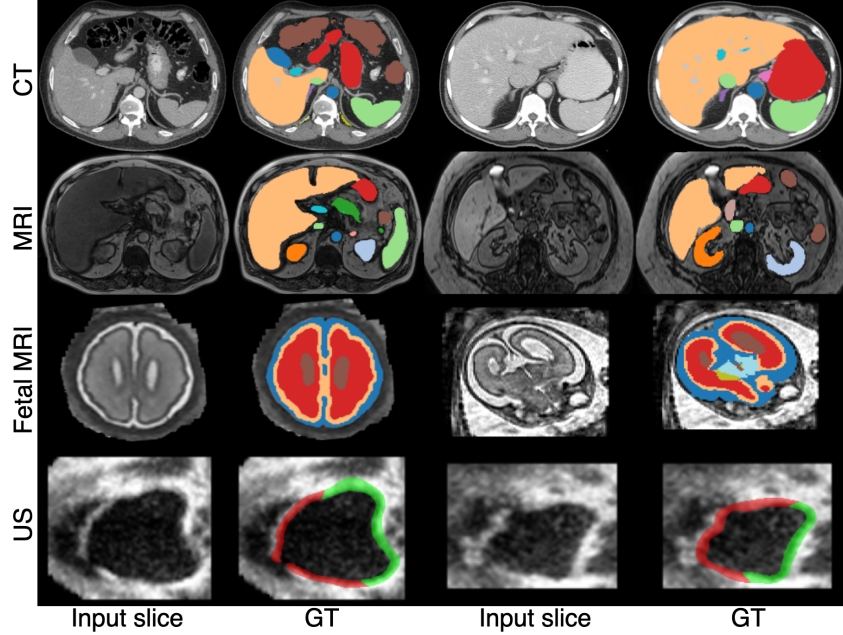


Figure 4: This figure provides an overview of the dataset used for pre-training, including CT scans (first row), MRI scans (second row), and Fetal MRI scans (third row), with 3D ultrasound (fourth row) specifically used for fine-tuning. The first and third columns, as well as the second and fourth columns, display independent input slices and corresponding ground truth for two cases. Although Fetal MRI and 3D ultrasound fall under the broader category of CT and MRI-based exams, this comparison highlights the distinct differences in feature representation between both CT And MRI and Fetal MRI with 3D US, showcasing variations in anatomical detail and imaging characteristics across these modalities.

We provide detailed quantitative results from the generalizability analysis. In this experiment, we train each network using the following protocols: (1) we train the model solely on the AMOS-CT training scans and evaluate it on the AMOS-CT validation set (see Table 12), (2) we train a model solely on the AMOS-MRI training scans and evaluate it on the AMOS-MRI validation set (see Table 15); (3) we train the model on the AMOS-MRI training scans with pre-training on the AMOS-CT training scans, and evaluate it on the AMOS-MRI validation set (see Table 16); and (4) we train the model on both the AMOS-CT and AMOS-MRI training scans, and evaluate it on both the AMOS-CT and AMOS-MRI validation sets (see Table 17).

Table 15: Qualitative results on AMOS-MRI validation set. We train each model solely on MRI data. We report mDSC (%) and mHD95 (mm) for each organ across all folds. Organs include Spleen (Sp), Right Kidney (RK), Left Kidney (LK), Gallbladder (GB), Esophagus (Es), Liver (Li), Stomach (St), Aorta (Ao), Inferior Vena Cava (IVC), Pancreas (Pa), Right Adrenal Gland (RAG), Left Adrenal Gland (LAG), Duodenum (Du), Bladder (Bl), and Prostate/Uterus (Pr/Ut). The best results are **bolded**, while the second-best are underlined. (*) indicates pre-trained model.

Method	DSC (%) \uparrow								
	Sp	RK	LK	GB	Es	Li	St	Ao	IVC
Hermes	95.5 \pm 2.3	95.4 \pm 1.1	95.3 \pm 1.1	68.0 \pm 22.1	72.3\pm11.4	96.7 \pm 1.5	83.4 \pm 13.8	90.2 \pm 5.4	87.2 \pm 4.0
Swin SMT	92.8 \pm 4.0	94.2 \pm 2.2	93.7 \pm 2.4	56.5 \pm 26.9	0.0 \pm 0.0	95.8 \pm 2.4	81.1 \pm 15.7	88.6 \pm 4.9	83.2 \pm 6.3
VSmTrans	94.8 \pm 2.0	94.3 \pm 3.6	94.9 \pm 2.2	65.3 \pm 24.9	69.7 \pm 9.2	96.6 \pm 1.6	83.8 \pm 16.2	<u>90.6\pm4.1</u>	85.5 \pm 6.1
SegMamba	95.6 \pm 1.9	95.1 \pm 1.7	95.3 \pm 1.4	64.3 \pm 27.2	70.2 \pm 11.4	96.9 \pm 1.1	<u>87.1\pm7.7</u>	91.2\pm4.1	86.6 \pm 6.0
uC 3DU-Net	91.6 \pm 5.6	92.6 \pm 2.9	93.4 \pm 2.4	71.0 \pm 25.5	67.1 \pm 12.1	95.0 \pm 4.1	83.2 \pm 13.6	89.0 \pm 6.1	83.4 \pm 7.3
Swin UNETR	93.5 \pm 4.2	94.5 \pm 2.5	94.7 \pm 1.9	70.3 \pm 22.5	68.2 \pm 9.4	96.3 \pm 2.6	84.4 \pm 14.1	90.2 \pm 4.5	86.0 \pm 4.5
SuPreM (*)	93.6 \pm 4.9	94.6 \pm 1.9	94.0 \pm 2.1	71.2 \pm 23.7	67.3 \pm 10.3	95.9 \pm 3.8	83.7 \pm 11.3	89.3 \pm 5.2	83.8 \pm 6.2
Mamba-HoME	95.2 \pm 2.1	94.6 \pm 2.1	94.6 \pm 2.4	<u>67.6\pm27.5</u>	<u>70.6\pm9.4</u>	<u>96.7\pm1.5</u>	<u>85.0\pm10.7</u>	90.0 \pm 5.1	87.6\pm5.0
Mamba-HoME (*)	96.1\pm1.3	95.5\pm1.1	95.7\pm0.9	75.3\pm22.4	72.3\pm8.9	97.5\pm0.5	89.1\pm6.7	90.4 \pm 5.4	86.5 \pm 5.4

Method	DSC (%) \uparrow						mDSC (%) \uparrow	mHD95 (mm) \downarrow
	Pa	RAG	LAG	Du	Bl	Pr/Ut		
Hermes	79.2 \pm 19.5	61.9 \pm 10.8	<u>60.8\pm16.9</u>	63.1 \pm 14.3	NA	NA	80.7 \pm 17.9	13.9\pm33.5
Swin SMT	79.4 \pm 12.5	0.0 \pm 0.0	0.0 \pm 0.0	56.3 \pm 13.0	NA	NA	63.2 \pm 38.2	45.1 \pm 72.7
VSmTrans	80.3 \pm 16.7	52.4 \pm 17.4	0.0 \pm 0.0	61.5 \pm 16.4	NA	NA	74.6 \pm 28.3	30.6 \pm 53.8
SegMamba	80.2 \pm 18.3	56.3 \pm 18.4	59.8 \pm 13.7	63.7 \pm 13.9	NA	NA	80.2 \pm 19.2	33.1 \pm 52.2
uC 3DU-Net	79.4 \pm 16.1	0.0 \pm 0.0	0.0 \pm 0.0	59.8 \pm 14.1	NA	NA	68.6 \pm 35.2	<u>16.3\pm28.5</u>
Swin UNETR	80.5 \pm 15.3	54.5 \pm 12.3	0.0 \pm 0.0	61.5 \pm 16.0	NA	NA	75.0 \pm 27.5	30.7 \pm 51.4
SuPreM (*)	79.8 \pm 15.0	0.0 \pm 0.0	0.0 \pm 0.0	60.6 \pm 13.0	NA	NA	70.3 \pm 33.4	52.1 \pm 69.8
Mamba-HoME	<u>81.6\pm15.6</u>	62.7\pm12.1	60.5 \pm 11.6	<u>65.8\pm13.8</u>	NA	NA	81.0 \pm 17.4	32.5 \pm 52.3
Mamba-HoME (*)	85.3\pm9.8	58.2 \pm 15.7	62.1\pm9.7	65.9\pm13.8	NA	NA	82.3\pm16.7	19.5 \pm 31.2

Table 16: Qualitative results on AMOS-MRI validation set, pre-trained on AMOS-CT dataset (CT \rightarrow MRI). We report mDSC (%) and mHD95 (mm) for each organ across all folds. Organs include Spleen (Sp), Right Kidney (RK), Left Kidney (LK), Gallbladder (GB), Esophagus (Es), Liver (Li), Stomach (St), Aorta (Ao), Inferior Vena Cava (IVC), Pancreas (Pa), Right Adrenal Gland (RAG), Left Adrenal Gland (LAG), Duodenum (Du), Bladder (Bl), and Prostate/Uterus (Pr/Ut). The best results are **bolded**, while the second-best are underlined. (*) indicates pre-trained model.

Method	DSC (%) \uparrow								
	Sp	RK	LK	GB	Es	Li	St	Ao	IVC
Hermes	96.6\pm1.2	95.8\pm0.8	96.0 \pm 0.7	77.7 \pm 27.7	78.3\pm6.3	97.7 \pm 0.7	90.4 \pm 8.5	92.5\pm3.8	89.9 \pm 2.9
Swin SMT	96.1 \pm 1.2	95.4 \pm 0.9	95.7 \pm 0.7	75.7 \pm 19.3	75.2 \pm 7.4	97.3 \pm 0.7	88.2 \pm 10.3	91.7 \pm 3.5	89.1 \pm 3.2
VSmTrans	96.2 \pm 1.3	95.8\pm0.8	95.7 \pm 0.7	79.9 \pm 18.3	74.1 \pm 7.8	87.5 \pm 0.6	90.5 \pm 4.9	91.2 \pm 4.2	89.5 \pm 2.9
SegMamba	94.7 \pm 2.9	95.0 \pm 1.8	95.0 \pm 1.4	67.4 \pm 22.7	69.9 \pm 9.7	96.3 \pm 2.3	84.3 \pm 13.0	90.5 \pm 3.0	84.7 \pm 6.6
uC 3DU-Net	96.1 \pm 1.4	95.8\pm0.8	95.8 \pm 0.7	80.1\pm21.2	76.8 \pm 8.2	97.3 \pm 1.0	88.5 \pm 10.1	91.8 \pm 3.9	89.1 \pm 3.1
Swin UNETR	96.1 \pm 1.1	95.6 \pm 0.7	95.8 \pm 0.6	78.9 \pm 15.5	72.4 \pm 7.6	97.2 \pm 0.8	89.2 \pm 6.5	91.0 \pm 4.1	88.9 \pm 3.0
SuPreM	96.1 \pm 1.9	95.3 \pm 2.0	95.8 \pm 0.7	76.7 \pm 22.5	73.9 \pm 7.4	97.5 \pm 0.7	88.9 \pm 9.1	91.8 \pm 3.7	88.8 \pm 3.3
Mamba-HoME	96.4 \pm 1.4	95.5 \pm 0.9	95.9 \pm 0.6	77.3 \pm 22.2	76.2 \pm 8.7	97.5 \pm 0.7	<u>90.9\pm5.0</u>	91.4 \pm 5.5	89.4 \pm 2.9
Mamba-HoME (*)	<u>96.5\pm1.3</u>	95.8\pm0.9	96.1\pm0.7	79.5 \pm 22.7	<u>77.0\pm8.1</u>	97.8\pm0.6	91.2\pm5.1	<u>92.4\pm3.0</u>	90.4\pm2.8

Method	DSC (%) \uparrow						mDSC (%) \uparrow	mHD95 (mm) \downarrow
	Pa	RAG	LAG	Du	Bl	Pr/Ut		
Hermes	86.0 \pm 12.9	65.2 \pm 9.9	63.5 \pm 16.0	72.0 \pm 13.3	NA	NA	84.8 \pm 16.0	11.9\pm20.1
Swin SMT	82.3 \pm 18.4	62.9 \pm 13.5	65.2 \pm 12.6	65.9 \pm 13.8	NA	NA	83.2 \pm 16.1	21.0 \pm 41.7
VSmTrans	85.4 \pm 12.6	64.2 \pm 9.6	66.8 \pm 9.3	70.8 \pm 11.7	NA	NA	84.5 \pm 14.2	30.1 \pm 55.3
SegMamba	80.8 \pm 14.6	57.0 \pm 15.3	50.5 \pm 17.1	60.6 \pm 13.7	NA	NA	79.0 \pm 19.4	14.7 \pm 26.6
uC 3DU-Net	84.3 \pm 16.0	63.8 \pm 10.8	68.4 \pm 9.0	71.0 \pm 13.2	NA	NA	84.5 \pm 14.8	15.4 \pm 25.8
Swin UNETR	85.1 \pm 13.8	65.9\pm9.1	69.3\pm8.2	68.6 \pm 15.4	NA	NA	84.2 \pm 14.1	28.4 \pm 57.7
SuPreM	85.2 \pm 13.4	63.5 \pm 13.9	66.5 \pm 15.4	71.0 \pm 13.1	NA	NA	83.9 \pm 15.7	14.8 \pm 26.9
Mamba-HoME	86.4\pm12.1	64.5 \pm 9.9	66.7 \pm 10.5	72.2\pm12.8	NA	NA	<u>84.8\pm14.7</u>	16.0 \pm 37.3
Mamba-HoME (*)	85.4 \pm 17.1	63.9 \pm 11.1	66.5 \pm 12.2	<u>72.0\pm14.2</u>	NA	NA	85.0\pm15.5	13.3 \pm 30.1

Table 17: Qualitative results on AMOS-CT + AMOS-MRI validation sets. We train each model on both CT and MRI training sets and evaluate on both CT and MRI validation sets. We report mDSC (%) and mHD95 (mm) for each organ across all folds. Organs include Spleen (Sp), Right Kidney (RK), Left Kidney (LK), Gallbladder (GB), Esophagus (Es), Liver (Li), Stomach (St), Aorta (Ao), Inferior Vena Cava (IVC), Pancreas (Pa), Right Adrenal Gland (RAG), Left Adrenal Gland (LAG), Duodenum (Du), Bladder (Bl), and Prostate/Uterus (Pr/Ut). The best results are **bolded**, while the second-best are underlined. (*) indicates pre-trained model.

Method	DSC (%) \uparrow								
	Sp	RK	LK	GB	Es	Li	St	Ao	IVC
Hermes	94.5 \pm 2.3	93.7 \pm 4.1	93.3 \pm 2.0	77.8 \pm 20.5	77.6 \pm 11.5	93.8 \pm 8.8	87.2 \pm 14.6	92.5 \pm 4.4	87.7 \pm 5.4
Swin SMT	91.1 \pm 12.8	94.0 \pm 4.6	94.2 \pm 4.1	75.1 \pm 23.8	76.7 \pm 13.0	94.0 \pm 8.4	79.2 \pm 21.4	90.8 \pm 6.2	85.6 \pm 12.2
VSmTrans	85.0 \pm 27.5	87.1 \pm 22.7	89.1 \pm 18.5	71.7 \pm 30.3	73.9 \pm 21.2	86.3 \pm 25.1	74.5 \pm 29.5	87.5 \pm 17.2	79.2 \pm 24.0
SegMamba	94.9 \pm 6.7	94.0 \pm 5.9	93.5 \pm 7.2	76.7 \pm 23.5	79.7 \pm 11.8	94.5 \pm 8.5	89.1 \pm 11.7	93.1\pm4.3	88.3\pm4.4
uC 3DU-Net	95.0 \pm 3.7	94.5 \pm 3.3	93.8 \pm 7.5	76.3 \pm 23.9	78.8 \pm 12.5	95.3 \pm 6.2	86.9 \pm 14.0	92.7 \pm 4.0	87.6 \pm 4.6
Swin UNETR	92.1 \pm 12.5	94.8 \pm 3.3	94.6 \pm 3.8	78.1 \pm 22.1	76.8 \pm 13.5	95.1 \pm 6.4	86.5 \pm 13.8	91.8 \pm 5.2	84.7 \pm 10.7
SuPreM	92.8 \pm 11.4	92.6 \pm 13.1	94.1 \pm 5.5	78.5 \pm 22.7	78.1 \pm 13.1	93.2 \pm 13.8	84.4 \pm 18.9	92.3 \pm 5.1	84.5 \pm 14.0
Mamba-HoME	95.2\pm4.5	<u>95.1\pm2.1</u>	<u>94.6\pm4.2</u>	<u>79.3\pm21.4</u>	<u>79.9\pm10.8</u>	<u>95.4\pm7.4</u>	<u>89.1\pm11.7</u>	92.8 \pm 4.4	88.2 \pm 4.3
Mamba-HoME (*)	<u>95.0\pm6.9</u>	95.3\pm2.6	95.6\pm1.8	82.7\pm19.5	80.0\pm12.6	96.3\pm2.8	90.4\pm10.8	<u>93.0\pm4.5</u>	87.8 \pm 6.2

Method	mDSC (%) \uparrow						mHD95 (mm) \downarrow	
	Pa	RAG	LAG	Du	Bl	Pr/Ut		
Hermes	82.0 \pm 13.8	71.7 \pm 13.5	70.0 \pm 16.2	72.2 \pm 15.4	83.3 \pm 20.0	79.3 \pm 17.3	82.9 \pm 15.3	36.1 \pm 80.7
Swin SMT	80.3 \pm 13.4	68.1 \pm 16.5	70.3 \pm 13.0	68.8 \pm 17.6	70.3 \pm 23.3	76.8 \pm 15.7	81.2 \pm 17.6	98.9 \pm 148.3
VSmTrans	74.5 \pm 24.0	64.3 \pm 25.9	67.2 \pm 21.7	67.3 \pm 25.8	82.6 \pm 19.3	80.8 \pm 12.0	78.0 \pm 24.9	102.1 \pm 131.8
SegMamba	83.1 \pm 12.0	68.5 \pm 16.2	72.5 \pm 13.7	76.0 \pm 14.8	83.4 \pm 19.8	82.3 \pm 14.9	84.7 \pm 15.3	64.2 \pm 124.9
uC 3DU-Net	81.9 \pm 12.4	71.7 \pm 14.0	70.7 \pm 15.4	74.0 \pm 15.8	83.2 \pm 19.4	76.7 \pm 20.3	84.1 \pm 15.8	34.9 \pm 78.7
Swin UNETR	82.8 \pm 12.8	69.1 \pm 13.9	71.0 \pm 15.0	74.6 \pm 17.3	83.1 \pm 18.8	81.5 \pm 13.7	83.8 \pm 15.7	84.7 \pm 145.1
SuPreM	82.3 \pm 12.5	67.8 \pm 19.4	71.9 \pm 13.9	74.2 \pm 16.5	84.4 \pm 18.2	81.2 \pm 13.4	83.5 \pm 16.7	48.2 \pm 86.3
Mamba-HoME	82.7 \pm 12.2	71.9 \pm 13.5	<u>72.7\pm13.4</u>	75.5 \pm 13.7	82.7 \pm 20.8	80.5 \pm 16.7	<u>85.1\pm14.6</u>	54.8 \pm 75.2
Mamba-HoME (*)	84.5\pm11.7	72.1\pm12.9	72.9\pm13.7	77.7\pm14.3	89.0\pm14.5	83.2\pm15.8	86.4\pm13.8	27.7\pm61.2

E Ablation studies

We provide detailed quantitative results from ablation studies. Specifically, we investigate three aspects: (1) the impact of the number of experts per stage, (2) the impact of group size, and (3) the impact of the number of slots per expert.

E.1 Effect of the number of experts

Table 18: Quantitative results of the effect of the number of experts on the PANORAMA test sets. We report mDSC (%) and HD95 (mm) for PDAC and Pancreas classes across datasets (NIH, MSD, in-house) and overall. Results are provided for pancreas in NIH, PDAC and pancreas in MSD, in-house, and overall. Note: NIH dataset contains only the Pancreas class. The best results are **bolded**, while the second-best are underlined. (*) indicates a doubled number of experts in the second level.

Experts (E)	NIH	MSD		In-house		Overall		mDSC (%) \uparrow	mHD95 (mm) \downarrow
	Pancreas	PDAC	Pancreas	PDAC	Pancreas	PDAC	Pancreas		
[4, 8, 12, 16]	92.6 \pm 2.4	51.2\pm30.4	88.4 \pm 7.0	60.8\pm26.8	81.7 \pm 11.2	54.8\pm29.5	88.3 \pm 8.1	77.5\pm21.2	6.9\pm12.1
[8, 16, 24, 48]	92.6 \pm 2.5	49.4 \pm 32.1	88.2 \pm 7.2	59.6 \pm 28.3	80.6 \pm 13.2	53.3 \pm 31.2	87.9 \pm 8.8	76.3 \pm 25.0	8.4 \pm 14.2
[8, 16, 24, 48]*	92.1 \pm 3.5	47.9 \pm 34.3	88.0 \pm 9.1	57.4 \pm 31.2	80.5 \pm 15.4	52.2 \pm 32.2	87.5 \pm 8.9	75.8 \pm 26.2	9.5 \pm 15.2
[16, 32, 48, 64]	92.7\pm2.2	<u>51.0\pm31.2</u>	88.5\pm7.1	<u>60.4\pm28.1</u>	81.9\pm11.0	<u>54.5\pm28.5</u>	88.4\pm8.2	77.5\pm21.5	<u>7.2\pm14.1</u>

Table 19: Quantitative results of AMOS CT validation dataset. We report mDSC (%) and mHD95 (mm) for each organ across all folds. Organs include Spleen (Sp), Right Kidney (RK), Left Kidney (LK), Gallbladder (GB), Esophagus (Es), Liver (Li), Stomach (St), Aorta (Ao), Inferior Vena Cava (IVC), Pancreas (Pa), Right Adrenal Gland (RAG), Left Adrenal Gland (LAG), Duodenum (Du), Bladder (Bl), and Prostate/Uterus (Pr/Ut). The best results are **bolded**, while the second-best are underlined. (*) indicates a doubled number of experts in the second level.

Experts (E)	DSC (%) ↑								
	Sp	RK	LK	GB	Es	Li	St	Ao	IVC
[4, 8, 12, 16]*	95.7±4.1	95.3±2.8	95.1±3.2	81.4±20.3	81.5±11.9	93.1±12.1	88.7±13.6	93.6±4.8	88.4±4.4
[8, 16, 24, 48]	<u>95.7±4.2</u>	93.7±6.4	94.0±7.0	81.0±20.8	81.5±13.1	95.3±7.0	89.3±13.6	93.2±4.9	88.4±4.4
[8, 16, 24, 48]*	94.7±6.0	95.4±2.7	95.0±3.6	81.6±20.9	81.4±12.3	95.4±6.4	87.0±15.0	93.4±4.8	87.8±5.1
[16, 32, 48, 64]	95.8±3.7	93.8±4.3	94.8±6.0	80.0±22.4	83.0±10.1	95.7±4.8	87.5±15.0	93.6±4.6	88.4±4.4

Experts (E)	mDSC (%) ↑						HD95 (mm) ↓	
	Pa	RAG	LAG	Du	Bl	Pr/Ut		
[4, 8, 12, 16]*	83.6±11.1	74.1±11.7	75.2±11.1	77.4±14.1	86.3±17.7	83.2±13.8	86.3±13.5	45.0±85.1
[8, 16, 24, 48]	83.4±11.2	73.8±12.0	<u>75.0±13.0</u>	77.6±14.3	87.6±16.8	83.3±15.5	86.2±13.9	<u>49.2±91.2</u>
[8, 16, 24, 48]*	83.4±11.9	73.8±11.6	74.4±12.4	77.0±12.6	86.0±17.1	82.2±16.3	85.9±13.9	55.6±75.2
[16, 32, 48, 64]	83.8±11.0	75.0±11.3	74.5±12.5	<u>77.5±13.5</u>	85.7±17.3	82.4±16.9	86.1±13.9	50.3±84.2

Table 20: 5-fold cross-validation on the FeTA 2022 dataset of the varying number of experts of HoME layer at each encoder stage. We report mDSC (%) and mHD95 (mm) for each class and across all folds. Results are provided for external cerebrospinal fluid (eCSF), gray matter (GM), white matter (WM), ventricles (V), cerebellum (C), deep gray matter (dGM), and brainstem (B). The best results are **bolded**, while the second-best are underlined. (*) indicates a doubled number of experts in the second level.

Experts (E)	DSC (%) ↑							mDSC (%) ↑	HD95 (mm) ↓
	eCSF	GM	WM	V	C	dGM	B		
[4, 8, 12, 16]	80.6±5.9	75.3±3.1	91.2±1.4	88.2±1.3	88.3±1.5	89.3±1.8	86.7±1.6	87.5±1.2	2.2±0.4
[8, 16, 24, 48]	80.4±6.2	75.1±3.4	91.1±1.5	88.3±1.2	88.5±1.2	88.6±2.1	86.6±1.5	87.2±1.4	2.4±0.5
[8, 16, 24, 48]*	80.7±5.7	75.5±3.2	91.1±1.5	<u>88.4±1.2</u>	88.5±1.8	89.4±1.4	86.9±1.6	<u>87.4±1.5</u>	<u>2.3±0.4</u>
[16, 32, 48, 64]	80.5±5.7	<u>75.4±3.4</u>	91.5±1.2	88.5±1.6	88.0±1.4	88.9±1.7	86.5±1.7	<u>87.4±1.6</u>	<u>2.3±0.5</u>

E.2 Effect of the groups size

Effect of varying group sizes across encoder stages 1–4 in a two-level HoME with constant experts [16, 32, 48, 64] and 4 slots per expert.

Table 21: Quantitative results of the effect of the number of slots per Expert. Mean Dice Similarity Coefficient (DSC, %) and 95th percentile Hausdorff Distance (HD95, mm) are reported for PDAC and Pancreas classes across datasets (NIH, MSD, in-house) and overall. Results are provided for pancreas in NIH, PDAC and pancreas in MSD, in-house, and overall. The best results are **bolded**, while the second-best are underlined. (*) indicates a doubled number of experts in the second level.

Group size (K)	NIH	MSD		In-house		Overall		mDSC (%) ↑	mHD95 (mm) ↓
	Pancreas	PDAC	Pancreas	PDAC	Pancreas	PDAC	Pancreas		
[1024, 512, 256, 128]	92.5±2.6	50.4±30.2	88.2±6.4	60.5±27.1	81.5±10.5	54.2±30.5	88.1±8.0	77.2±24.7	9.2±5.1
[2048, 1024, 512, 256]	92.9±2.2	51.2±30.5	88.4±7.0	60.8±26.8	81.7±11.2	54.8±29.5	88.3±8.1	77.5±23.8	6.9±4.0
[2048, 1024, 512, 256]*	<u>92.7±2.7</u>	50.3±31.5	88.3±7.0	56.3±29.1	81.7±10.9	52.6±30.8	88.2±8.0	76.8±25.0	11.2±5.7
[4096, 2048, 1024, 512]	92.5±2.5	51.9±30.2	88.1±6.6	<u>60.6±27.0</u>	81.5±10.7	55.2±29.3	88.0±7.7	77.4±23.5	<u>7.2±4.2</u>

Table 22: Quantitative results of AMOS CT validation dataset. Mean Dice Similarity Coefficient (DSC) (%) and 95th percentile Hausdorff Distance (HD95) (mm) are reported for each organ across all folds. Organs include Spleen (Sp), Right Kidney (RK), Left Kidney (LK), Gallbladder (GB), Esophagus (Es), Liver (Li), Stomach (St), Aorta (Ao), Inferior Vena Cava (IVC), Pancreas (Pa), Right Adrenal Gland (RAG), Left Adrenal Gland (LAG), Duodenum (Du), Bladder (Bl), and Prostate/Uterus (Pr/Ut). The best results are **bolded**, while the second-best are underlined. (*) indicates a doubled number of experts in the second level.

Group size (K)	DSC (%) ↑								
	Sp	RK	LK	GB	Es	Li	St	Ao	IVC
[4096, 2048, 1024, 512]	95.7±3.8	95.1±3.3	95.5±2.7	81.2±20.3	82.0±10.8	89.0±18.6	86.5±16.5	93.5±4.1	87.8±5.7
[2048, 1024, 512, 256]	95.8±3.7	93.8±4.3	94.8±6.0	80.0±22.4	83.0±10.1	95.7±4.8	87.5±15.0	93.6±4.6	88.4±4.4
[2048, 1024, 512, 256]*	95.5±3.4	95.2±3.1	95.6±2.5	81.0±18.2	82.1±10.2	89.1±16.6	86.2±14.2	93.2±4.4	87.5±5.9
[1024, 512, 256, 128]	95.5±3.9	95.4±3.5	94.85±2.5	81.5±17.2	<u>82.1±9.9</u>	<u>89.1±16.8</u>	86.4±15.4	93.4±4.2	87.6±4.9

Group size (K)	DSC (%) ↑						mDSC (%) ↑	HD95 (mm) ↓
	Pa	RAG	LAG	Du	Bl	Pr/Ut		
[4096, 2048, 1024, 512]	82.8±12.2	73.3±12.4	75.0±12.9	76.4±14.1	87.8±16.1	82.0±16.1	86.1±14.7	48.4±87.2
[2048, 1024, 512, 256]	83.8±11.0	75.0±11.3	74.5±12.5	77.5±13.5	85.7±17.3	82.4±16.9	86.3±13.9	45.0±85.1
[2048, 1024, 512, 256]*	83.9±10.8	75.2±11.0	75.1±12.2	77.3±13.1	85.6±17.1	82.1±16.0	86.2±14.7	48.2±83.7
[1024, 512, 256, 128]	82.8±13.1	73.1±13.5	75.1±12.4	76.1±15.1	<u>87.5±16.7</u>	<u>82.1±17.2</u>	86.1±15.2	51.4±83.2

Table 23: 5-fold cross-validation on the FeTA 2022 dataset of the varying number of groups at each encoder stage. We report mDSC (%) and mHD95 (mm) for each class and across all folds. Results are provided for external cerebrospinal fluid (eCSF), gray matter (GM), white matter (WM), ventricles (V), cerebellum (C), deep gray matter (dGM), and brainstem (B). The best results are **bolded**, while the second-best are underlined. (*) indicates a doubled number of experts in the second level.

Group size (K)	DSC (%) ↑							mDSC (%) ↑	HD95 (mm) ↓
	eCSF	GM	WM	V	C	dGM	B		
[4096, 2048, 1024, 512]	80.5±5.7	75.1±3.1	91.1±1.5	88.1±1.4	88.2±1.7	89.6±1.9	86.8±2.0	87.4±1.2	2.2±0.3
[2048, 1024, 512, 256]	80.6±5.9	<u>75.3±3.1</u>	91.2±1.4	88.2±1.3	<u>88.3±1.5</u>	89.3±1.8	86.7±1.6	87.5±1.2	2.2±0.4
[2048, 1024, 512, 256]*	80.4±5.7	75.3±2.9	91.0±1.6	88.0±1.4	88.5±1.6	89.3±1.7	86.3±1.8	87.3±1.1	<u>2.3±0.4</u>
[1024, 512, 256, 128]	80.4±5.1	75.7±2.7	90.3±1.5	87.2±1.7	88.3±1.7	<u>89.4±1.8</u>	87.0±1.4	<u>87.4±1.1</u>	<u>2.3±0.3</u>

E.3 Effect of the number of slots

Table 24: Quantitative results of the effect of the number of slots per expert. We report mDSC (%) and mHD95 (mm) for PDAC and Pancreas classes across datasets (NIH, MSD, in-house) and overall. Results are provided for pancreas in NIH, PDAC, and pancreas in MSD, in-house, and overall. The best results are **bolded**, while the second-best are underlined. (*) indicates a doubled number of experts in the second level.

Slots (S)	NIH	MSD		In-house		Overall		mDSC (%) ↑	mHD95 (mm) ↓
	Pancreas	PDAC	Pancreas	PDAC	Pancreas	PDAC	Pancreas		
1	93.0±2.1	46.6±32.4	88.6±6.4	55.9±31.4	82.2±10.9	50.1±32.3	88.5±7.6	76.2±26.4	9.2±5.1
2	92.5±2.8	49.7±31.1	88.0±7.4	61.5±26.6	82.0±11.2	54.2±30.0	88.0±8.2	77.2±24.2	7.4±4.5
4	<u>92.9±2.2</u>	51.2±30.5	88.4±7.0	60.8±26.8	81.7±11.2	54.8±29.5	88.3±8.1	77.5±23.8	6.9±3.9
8	92.8±2.5	46.4±32.5	88.3±6.8	60.6±27.3	81.3±11.6	51.8±31.4	88.1±8.1	76.5±25.5	8.7±5.0

Table 25: Qualitative results of the effect of the number of slots per expert on AMOS2022 CT validation set. Mean Dice Similarity Coefficient (DSC) (%) and 95th percentile Hausdorff Distance (HD95) (mm) are reported for each organ across all folds. Organs include Spleen (Sp), Right Kidney (RK), Left Kidney (LK), Gallbladder (GB), Esophagus (Es), Liver (Li), Stomach (St), Aorta (Ao), Inferior Vena Cava (IVC), Pancreas (Pa), Right Adrenal Gland (RAG), Left Adrenal Gland (LAG), Duodenum (Du), Bladder (Bl), and Prostate/Uterus (Pr/Ut). The best results are **bolded**, while the second-best are underlined.

Slots (S)	DSC (%) \uparrow								
	Sp	RK	LK	GB	Es	Li	St	Ao	IVC
1	95.0 \pm 5.0	93.0 \pm 8.1	95.1 \pm 3.2	80.6\pm22.0	81.4 \pm 11.9	95.7 \pm 5.8	87.4 \pm 15.1	93.5 \pm 4.9	88.8 \pm 4.3
2	95.5\pm3.9	95.3 \pm 3.4	95.1 \pm 4.5	<u>80.3\pm19.7</u>	<u>82.3\pm9.9</u>	91.3 \pm 15.9	87.7 \pm 15.9	93.7\pm4.4	88.9\pm4.1
4	95.5\pm4.1	96.0\pm1.5	95.5\pm2.8	79.7 \pm 21.1	82.4\pm10.1	96.1\pm3.8	87.8\pm15.1	93.4 \pm 4.2	88.7 \pm 4.2
8	<u>95.3\pm4.3</u>	<u>95.8\pm1.6</u>	<u>95.3\pm3.0</u>	79.5 \pm 22.2	82.3 \pm 10.0	96.1\pm4.0	87.6 \pm 15.3	93.3 \pm 4.6	88.7 \pm 4.2

Slots (S)	DSC (%) \uparrow						mDSC (%) \uparrow	HD95 (mm) \downarrow
	Pa	RAG	LAG	Du	Bl	Pr/Ut		
1	84.4\pm10.8	75.0 \pm 12.0	74.8 \pm 12.2	<u>77.8\pm12.7</u>	83.8 \pm 19.0	82.4\pm15.1	85.9 \pm 14.0	54.4 \pm 25.3
2	84.0 \pm 10.9	74.6 \pm 11.2	74.5 \pm 14.3	78.6\pm12.8	86.2 \pm 16.3	81.3 \pm 16.6	86.0 \pm 14.0	52.4 \pm 26.5
4	82.4 \pm 12.1	75.2\pm11.2	75.5\pm10.2	76.3 \pm 14.1	87.6\pm14.6	<u>81.7\pm15.2</u>	86.3\pm13.9	45.0\pm23.1
8	82.2 \pm 12.5	74.9 \pm 11.8	<u>75.4\pm11.6</u>	76.2 \pm 14.3	87.6\pm15.7	81.6 \pm 16.0	<u>86.1\pm13.9</u>	<u>51.2\pm25.2</u>

Table 26: 5-fold cross-validation on the FeTA 2022 dataset of the varying number of slots per experts at each encoder stage. We report mDSC (%) and mHD95 (mm) for each class and across all folds. Results are provided for external cerebrospinal fluid (eCSF), gray matter (GM), white matter (WM), ventricles (V), cerebellum (C), deep gray matter (dGM), and brainstem (B). The best results are **bolded**, while the second-best are underlined.

Slots (S)	DSC (%) \uparrow							mDSC (%) \uparrow	HD95 (mm) \downarrow
	eCSF	GM	WM	V	C	dGM	B		
1	80.6 \pm 5.6	75.1 \pm 3.2	91.0 \pm 1.7	87.9 \pm 1.7	88.4 \pm 1.4	89.4 \pm 1.9	86.4 \pm 1.7	87.3 \pm 1.1	2.2 \pm 0.4
2	80.7\pm5.6	75.3\pm3.1	91.1 \pm 1.6	87.9 \pm 1.7	88.5 \pm 1.5	89.6\pm1.8	86.4 \pm 1.8	87.4 \pm 1.2	2.4 \pm 0.5
4	80.4 \pm 5.8	75.3\pm3.1	91.2\pm1.5	88.2\pm1.3	88.8\pm1.6	89.4 \pm 1.8	86.6\pm1.5	87.5\pm1.2	2.1\pm0.2
8	<u>80.5\pm5.6</u>	<u>75.3\pm3.0</u>	<u>91.1\pm1.5</u>	<u>88.1\pm1.3</u>	<u>88.5\pm1.2</u>	<u>89.5\pm1.7</u>	<u>88.6\pm1.7</u>	<u>87.4\pm1.2</u>	<u>2.1\pm0.3</u>

E.4 Impact of the HoME layer

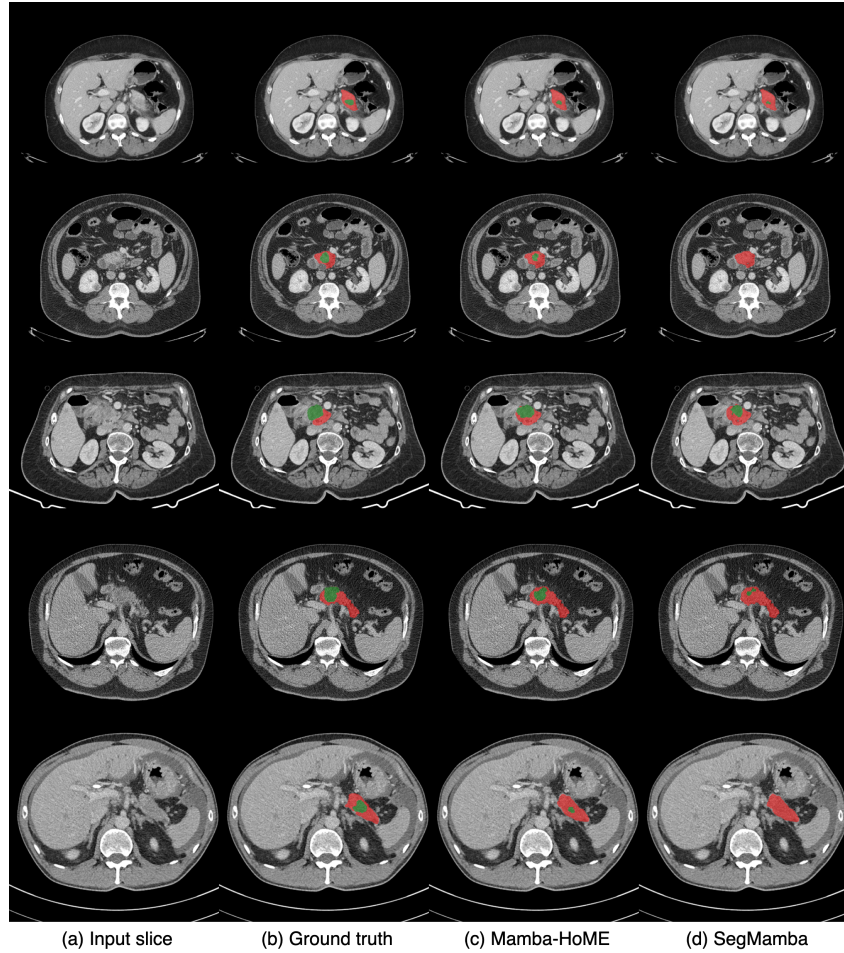


Figure 5: Qualitative comparison of Mamba-HoME and SegMamba on abdominal CT scans from PANORAMA test set. The images highlight the impact of the HoME layer added to the baseline SegMamba model, with green (PDAC) and red (pancreas) annotations indicating segmentation differences. Mamba-HoME demonstrates robustness and improved accuracy in detecting both small and large anatomical structures, like tumors, compared to SegMamba alone. Please note that we show Mamba-HoME results trained from scratch.

F Qualitative results

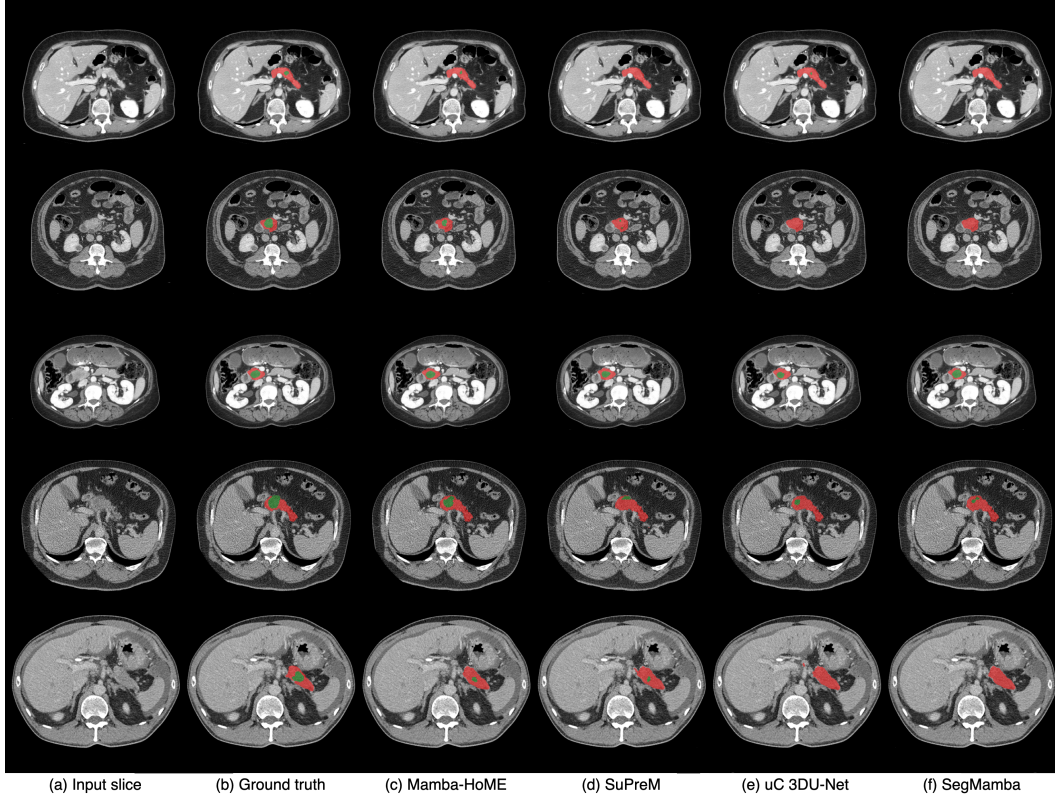


Figure 6: Qualitative segmentation results for PDAC (green) and the pancreas (red) provided by Mamba-HoME and the next three top-performing methods. The first three rows display cases from the Pancreas-MSD dataset, while the last two rows show cases from the in-house dataset. Please note, we show Mamba-HoME results trained from scratch.

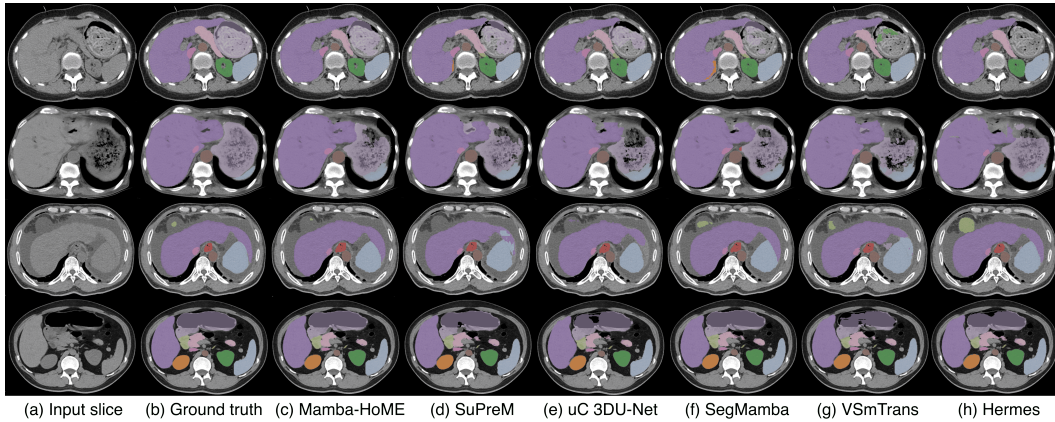


Figure 7: Qualitative segmentation results on the AMOS-CT validation set for Mamba-HoME (trained from scratch), SuPreM, uC 3DU-Net, SegMamba, VSmTrans, and Hermes. All models are trained on both the AMOS-CT and AMOS-MRI training datasets.

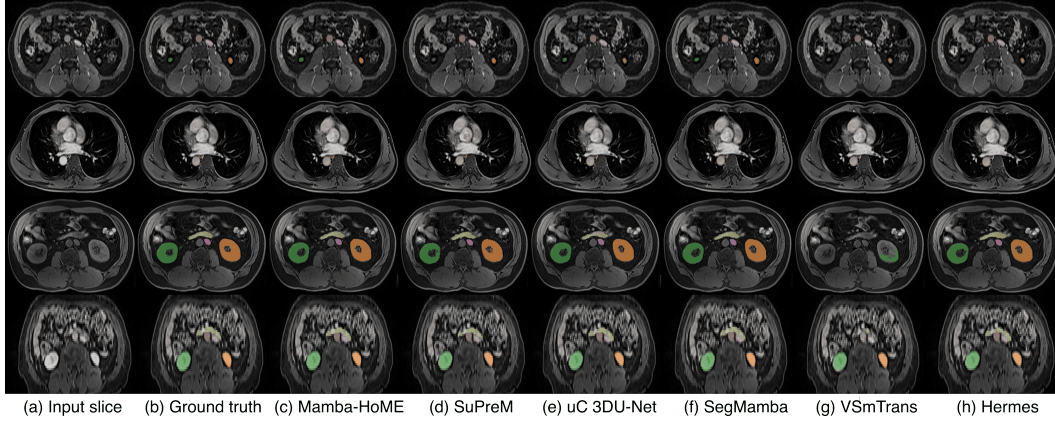


Figure 8: Qualitative comparison of segmentation performance on the AMOS-MRI validation set for six methods: Mamba-HoME (trained from scratch), SuPreM, uC 3DU-Net, SegMamba, VSmTrans, and Hermes. The models are trained on both training dataset of AMOS-CT and AMOS-MRI.

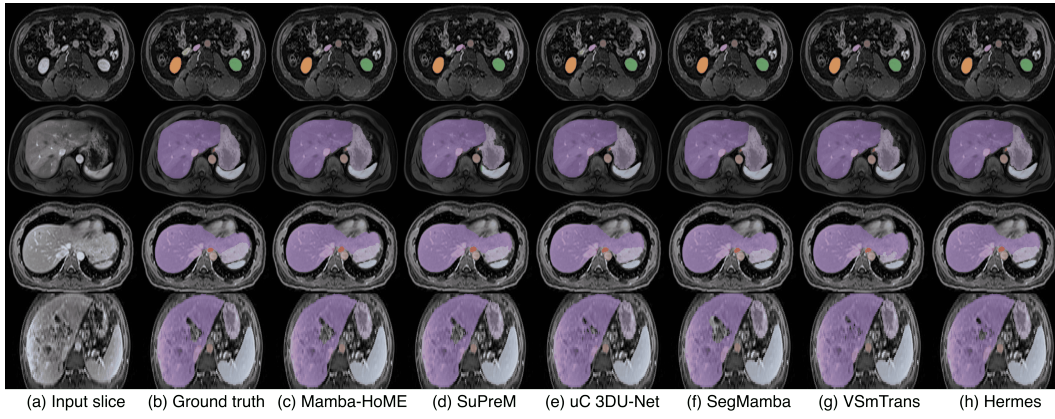


Figure 9: Qualitative segmentation results on the AMOS-MRI validation set for Mamba-HoME, SuPreM, uC 3DU-Net, SegMamba, VSmTrans, and Hermes. Models are first pre-trained on the AMOS-CT scans and subsequently fine-tuned on the AMOS-MRI training data.

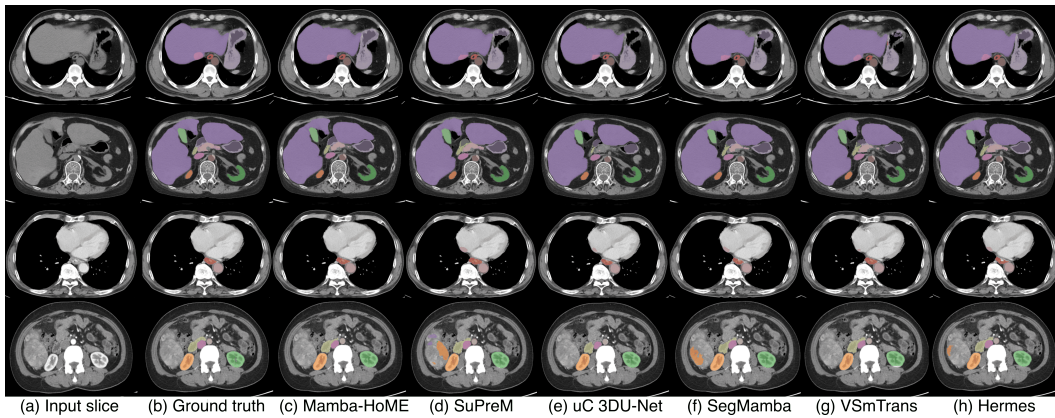


Figure 10: Qualitative segmentation results on the AMOS-CT validation set for Mamba-HoME, SuPreM, uC 3DU-Net, SegMamba, VSmTrans, and Hermes. Each model is trained only on the AMOS-CT training scans.

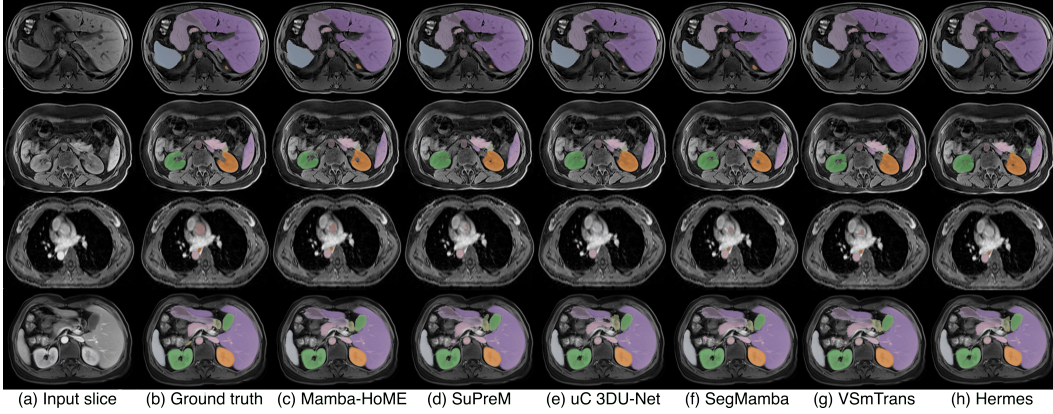


Figure 11: Qualitative segmentation results on the AMOS-MRI validation set for Mamba-HoME, SuPreM, uC 3DU-Net, SegMamba, VSmTrans, and Hermes. These models are trained solely on the AMOS-MRI training set.

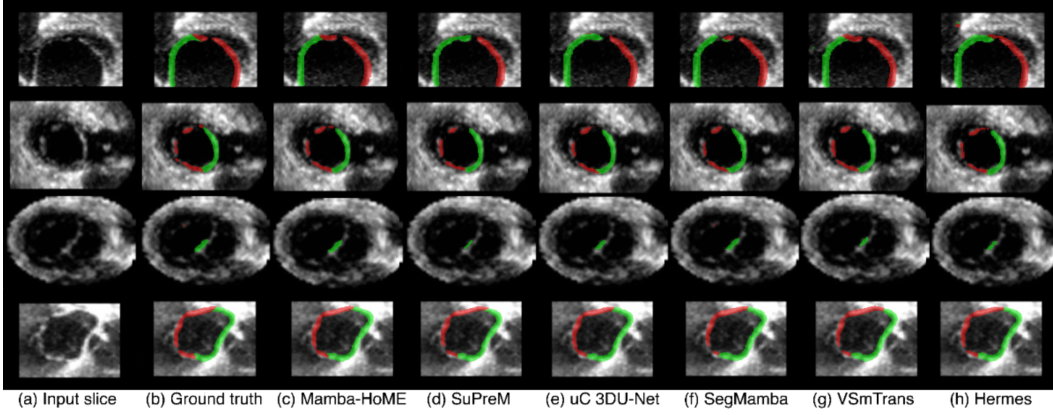


Figure 12: Qualitative segmentation results of Mamba-HoME, SuPreM, uC 3DU-Net, SegMamba, VSmTrans, and Hermes on the MVSeg2023 test set.

G Impact statement

This work introduces Hierarchical Soft Mixture-of-Experts (HoME), a novel architecture for efficient and accurate 3D medical image segmentation. By integrating a two-level mixture-of-experts routing mechanism with Mamba-based state space models, our method significantly advances long-context modeling for volumetric data. HoME is designed to address key challenges in medical imaging, namely, modeling local-to-global spatial hierarchies, handling modality diversity (CT, MRI, US), and achieving scalability for high-resolution 3D inputs. Our proposed Mamba-HoME architecture demonstrates strong generalization and outperforms state-of-the-art models across public and in-house datasets, while being memory and compute efficient.

Beyond medical imaging, the architectural principles introduced, specifically the hierarchical token routing and the integration of local and global context processing, are applicable to other domains dealing with structured, hierarchical data under resource constraints. These include scientific computing, robotics, and spatiotemporal analysis in environmental or geospatial datasets.

Ethically, this work supports equitable healthcare by enabling accurate segmentation with reduced computational requirements, which is crucial for deployment in low-resource settings. We use publicly available datasets and provide open-source code to ensure reproducibility and accessibility for the broader community. No personally identifiable information or sensitive patient data is used. Future extensions could include further robustness to distributional shifts in medical data and broader clinical evaluation.